

# 1 **Reply to Anonymous Referee**

2 We thank the reviewer for her/his positive review. We have addressed the reviewer's  
3 comments in the revised manuscript. The modification are marked in red.  
4

## 6 **Revised manuscript:**

### 8 **Effect of deep convection on the TTL composition over the** 9 **Southwest Indian Ocean during austral summer.**

10 Stephanie Evan<sup>1</sup>, Jerome Brioude<sup>1</sup>, Karen Rosenlof<sup>2</sup>, Sean. M. Davis<sup>2</sup>, **Holger** Vömel<sup>3</sup>, Damien Héron<sup>1</sup>,  
11 Françoise Posny<sup>1</sup>, Jean-Marc Metzger<sup>4</sup>, Valentin Duflot<sup>1,4</sup>, Guillaume Payen<sup>4</sup>, Hélène Vérémes<sup>1</sup>,  
12 Philippe Keckhut<sup>5</sup>, and Jean-Pierre Cammas<sup>1,4</sup>

13 <sup>1</sup>LACy, Laboratoire de l'Atmosphère et des Cyclones, UMR8105 (CNRS, Université de La Réunion, Météo-France), Saint-  
14 Denis de la Réunion, 97490, France

15 <sup>2</sup>Chemical Sciences Division, Earth System Research Laboratory, NOAA, Boulder, 80305, CO, USA

16 <sup>3</sup>National Center for Atmospheric Research, Boulder, 80301, CO, USA

17 <sup>4</sup>Observatoire des Sciences de l'Univers de La Réunion, UMS3365 (CNRS, Université de La Réunion, Météo-France), Saint-  
18 Denis de la Réunion, 97490, France

19 <sup>5</sup>LATMOS, Laboratoire ATmosphères, Milieux, Observations Spatiales-IPSL UMR8190 (UVSQ Université Paris-Saclay,  
20 Sorbonne Université, CNRS), Guyancourt, 78280, France

21 *Correspondence to:* Stephanie Evan (stephanie.evan@univ-reunion.fr)

22 **Abstract.** Balloon-borne measurements of CFH water vapor, ozone and temperature and water vapor lidar measurements  
23 from the Maïdo Observatory at Réunion Island in the Southwest Indian Ocean (SWIO) were used to study tropical cyclones'  
24 influence on TTL composition. The balloon launches were specifically planned using a Lagrangian model and METEOSAT  
25 7 infrared images to sample the convective outflow from Tropical Storm (TS) Coentim on 25 January 2016 and Tropical  
26 Cyclone (TC) Enawo on 3 March 2017.

27 Comparing CFH profile to MLS monthly climatologies, water vapor anomalies were identified. Positive anomalies of water  
28 vapor and temperature, and negative anomalies of ozone between 12 and 15 km in altitude (247 to 121hPa) originated from

29 convectively active regions of TS Corentin and TC Enawo, one day before the planned balloon launches, according to the  
30 Lagrangian trajectories.

31 Near the tropopause region, air masses on 25 January 2016 were anomalously dry around 100hPa and were traced back to  
32 TS Corentin active convective region where cirrus clouds and deep convective clouds may have dried the layer. An  
33 anomalously wet layer around 68 hPa was traced back to the South East IO where a monthly water vapor anomaly of  
34 0.5ppmv was observed. In contrast, no water vapor anomaly was found near or above the tropopause region on 3 March  
35 2017 over Maïdo as the tropopause region was not downwind of TC Enawo. This study compares and contrasts the impact of  
36 two tropical cyclones on the humidification of the TTL over the SWIO. It also demonstrates the need for accurate balloon-  
37 borne measurements of water vapor/ozone/aerosols in regions where TTL in-situ observations are sparse.

## 38 **1 Introduction**

39 Deep convection plays an important role in delivering water and other chemical constituents to the Tropical Tropopause  
40 Layer (TTL, ~14-19 km altitude, Fueglistaler et al., 2009) and lower stratosphere regions. Two important pathways for trace  
41 gas transport from the surface to the tropical stratosphere are i) deep convective injection directly into the stratosphere  
42 (Danielsen, 1982; Dessler and Sherwood, 2003), ii) convective detrainment into the TTL followed by a slow ascent into the  
43 stratosphere (Holton and Gettelman, 2001). Moist boundary layer air is transported to the upper troposphere by deep  
44 convection with the main outflow region at about 13 km (Folkins and Martin, 2005). However very deep convection may  
45 overshoot the 18 km level into the stratosphere, injecting water vapor and ice crystals directly (Corti et al., 2008; Khaykin et  
46 al., 2009; Avery et al., 2017). Studies based on Eulerian cloud resolving models have shown that those overshoots can  
47 moisten the lower stratosphere due to evaporation of ice crystals (Dauhut et al., 2015; Frey et al., 2015). However,  
48 convection can also cool the cold point tropopause (CPT) (Kuang and Bretherton, 2004), which can enhance dehydration via  
49 in-situ formation of cirrus clouds. In fact, the net impact of deep convection on TTL humidity (e.g. moistening versus  
50 dehydration) depends on the initial pre-convection TTL relative humidity with respect to ice (RHi) conditions and size of the  
51 ice crystals formed in the convective updrafts (Jensen et al., 2007; Ueyama et al., 2018). In sub-saturated TTL air, condensed  
52 ice is not removed quickly enough to produce net dehydration. Recent studies based on Lagrangian models (Schoeberl et al.,  
53 2014, Ueyama et al., 2015) that include convection and cirrus clouds microphysics show that convection impacts TTL cirrus  
54 clouds and water vapor near the tropical tropopause by 10-30% (~1 ppmv). Therefore, they concluded that convection is  
55 significant for the moisture budget of the TTL and must be included to fully model the dynamics and chemistry of the TTL  
56 and lower stratosphere.

57 As the exact role of convection in hydrating/dehydrating the stratosphere is still under debate, additional accurate TTL

58 observations and modeling work are still needed to quantify the overall impact of convection on TTL composition and  
59 climate. At the moment, a realistic representation of deep convection and its effects remains a challenge for most global  
60 scale climate models and numerical weather prediction models (NWP).

61 Our understanding of how deep convection controls TTL humidity and composition, to a large extent, results from  
62 experiments in South America, the Western Pacific and South-East Asia (e.g. Toon et al., 2010; Jensen et al., 2017;  
63 Brunamonti et al., 2018). The role of the Indian Ocean (IO) in the global climate system is less understood than that of the  
64 Pacific Ocean, which has been more intensively observed and studied.

65 The tropical Indian Ocean has seen an unprecedented rise in heat content and is now home to 70% of the global ocean heat  
66 gain in the upper 700 m of the ocean during the past decade (Lee et al., 2015). Liu and Zipser (2015) showed using radar  
67 observations from the Global Precipitation Measurement (GPM) satellite that deep convection deeper than 15 km (Figure 1  
68 of Liu and Zipser, 2015) can occur over the South IO with dozens of systems reaching above 17 km. These systems are  
69 likely tropical cyclones over the SWIO or thunderstorms that are often observed over Madagascar during austral summer  
70 (Roca et al., 2002; Bovalo et al.; 2012).

71 Tropical cyclones are unique among tropical and subtropical convective systems in that they persist for many days and  
72 hydrate a deep layer of the surrounding upper troposphere (Ray and Rosenlof, 2007). Ray and Rosenlof (2007) used  
73 measurements from AIRS to assess the impact of tropical cyclones in the Atlantic and Pacific basins on the amount of water  
74 vapor in the tropical UT. They showed that tropical cyclones can hydrate a deep layer of the surrounding upper troposphere  
75 by ~30-50 ppmv or more within 500 km of the eye compared to the surrounding average water vapor mixing ratios. In  
76 addition, a modelling study by Allison et al. (2018) for TC Ingrid (2013) in the Gulf of Mexico indicated overshooting  
77 convection within the cyclone and associated strong vertical motions that transported large quantities of vapor and ice to the  
78 lower stratosphere.

79 Using 11-year TRMM precipitation satellite observations, Tao and Jiang (2012) identified overshooting tops in tropical  
80 cyclones (above 14 km) and showed that the South IO is the second basin after the Northwest Pacific in terms of total  
81 number of overshooting tops (cf. Table 2 of Tao and Jiang, 2012). Even though convection occurs predominantly over land  
82 in the tropics, overshooting convection in tropical cyclones contributes ~15% of the total convection reaching the tropopause  
83 (Romps and Kuang, 2009).

84 The location of Réunion Island (21°S, 55°E) is thus ideal to study tropical cyclone effects on TTL composition. Réunion  
85 Island was formally designated as a Regional Specialized Meteorological Centre (RSMC) - Tropical Cyclones for the  
86 Southwestern Indian Ocean (SWIO, 0-40°S, 30-100°E) by the World Meteorological Organization (WMO) in 1993. The

87 RSMC Réunion Island is responsible for the monitoring of all the tropical systems occurring over its area of responsibility.  
88 The SWIO is the third most active tropical cyclone basin with an average of 9.3 tropical storms with  
89 maximum sustained winds  $\geq 63$  km/h forming each year (Neumann, 1993). In the SWIO basin, a storm  
90 system is called a tropical cyclone when wind speeds exceed 118 km/h.

91 We take advantage of the position of Réunion Island in the SWIO to study tropical cyclones' influence on TTL composition  
92 (water vapor/ozone) during austral summers 2016 and 2017. Austral summer (Nov-March) is the ideal time to sample  
93 convective outflow from tropical cyclones or mesoscale convective systems forming near Madagascar.

94 The present work is organized as follows. Section 2 has a description of the data used in this study. Section 3 presents the  
95 model used to infer the convective origin of the measurements. Section 4 presents the water vapor/ozone distributions over  
96 Réunion Island during the two storm events and thermodynamics of the troposphere and TTL. Section 5 discusses the  
97 convective influence on the measurements as inferred from an analysis of Lagrangian trajectories. The results are discussed  
98 in Section 6. Section 7 contains a summary of our study.

## 99 **2 Data**

### 100 **2.1 Balloon data**

101 Balloon-borne measurements of water vapor and temperature in coordination with ground-based instrumentation (lidars)  
102 started in 2014 at the Maïdo Observatory (21.08°S, 55.38°E) within the framework of the Global Climate Observing System  
103 (GCOS) Reference Upper-Air Network (GRUAN) network (Bodeker et al., 2016). The balloon sonde payload consists of the  
104 Cryogenic Frostpoint Hygrometer (CFH) and the Internet iMet-1-RSB radiosonde for data transmission. The iMet-1-RSB  
105 radiosonde provides measurements of pressure, temperature, Relative Humidity (RH) and wind data (speed and direction  
106 from which zonal and meridional winds are derived). The CFH was developed to provide highly accurate water vapor  
107 measurements in the TTL and stratosphere where the water vapor mixing ratios are extremely low ( $\sim 2$  ppmv). CFH mixing  
108 ratio measurement uncertainty ranges from 5% in the tropical lower troposphere to less than 10% in the stratosphere (Vömel  
109 et al., 2007b); a recent study shows that the uncertainty in the stratosphere can be as low as 2-3% (Vömel et al., 2016).  
110 **However, water vapor measurements in the stratosphere by the CFH can be contaminated by sublimation of water from an**  
111 **icy intake, or from the balloon and payload at a pressure lower than 20hPa (Jorge et al., 2020).** The iMET-1-RSB has a  
112 temperature measurement uncertainty of 0.3°C, or 5% in RH, with an altitude independent bias of  $0.5 \pm 0.2$  °C (Hurst et al.,  
113 2011). As for vertical coordinate, we use the geopotential height calculated from the iMet-1-RSB measurements of pressure,

114 temperature and RH. Hurst et al. (2011) reported altitude-dependent differences of -0.1 to -0.2 km above 20 km between the  
115 geopotential altitudes derived from the Vaisala RS92 and Internet iMet-1-RSB sondes. The CFH and iMet-1-RSB  
116 measurements have high vertical resolution (5-10m) and are binned in altitude intervals of 200 m to reduce measurement  
117 noise. Here we present CFH measurements (water vapor mixing ratio and Relative Humidity with respect to ice,  $RH_{ice}$ ) from  
118 2 soundings performed in austral summers 2016 and 2017, when deep convection was active near Réunion Island (tropical  
119 cyclones Corentin and Enawo, cf. Figure 1). During austral summer, balloon launch planning is optimized using a  
120 Lagrangian forecasting tool. 5-day backward Lagrangian trajectories initialized from the location of the Maïdo Observatory  
121 at different altitudes (9.5, 12.5, 15.5 and 18 km) are run twice-daily and superimposed on current geostationary infrared  
122 satellite images to identify on-going convection over the SWIO (<http://geosur.univ-reunion.fr/foot>). This allows the  
123 identification of air masses with a convective origin that can be measured at the Observatory, thereby maximizing local  
124 resources by only measuring when convectively influenced air masses will be sampled.

125 In addition to CFH measurements at the Observatory, weekly Network for the Detection of Atmospheric Composition  
126 Change (NDACC)/Southern Hemisphere ADditional OZonesondes (SHADOZ) ozonesondes (Thompson et al., 2003; Witte  
127 et al., 2017) are launched from the airport (Gillot: 21.06°S, 55.48°E), located on the north side of the island (the flying  
128 distance between the Maïdo Observatory and the airport is ~20km). The ozonesonde is flown with a Meteomodem M10  
129 radiosonde that provides meteorological variables such as temperature, pressure, relative humidity and winds. In this study,  
130 the NDACC/SHADOZ ozone and temperature measurements are reported in 200 m altitude bins.

## 131 **2.2 Water vapor lidar data**

132 A Raman water vapor lidar emitting at 355 nm has been operating at the Maïdo Observatory since April 2013 (Baray et al.,  
133 2013; Keckhut et al., 2015; Vérèmes et al., 2019). Laser pulses are generated by two Quanta Ray Nd:Yag lasers, the  
134 geometry for transmitter and receiver is coaxial and the backscattered signal is collected by a Newtonian telescope with a  
135 primary mirror of 1200 mm diameter. 387 nm ( $N_2$ ) and 407 nm ( $H_2O$ ) Raman shifted wavelengths are used to retrieve the  
136 water vapor mixing ratio. Depending on the scientific investigations, specific filter points and integration times can be  
137 chosen. The raw vertical resolution is 15 m. Data are smoothed with a low-pass filter using a Blackman window. Based on  
138 the number of points used for this filter to vertically average the data, the vertical resolutions are 100-200 m in the lowest  
139 layers, 500 m in the mid-troposphere, 600 m in the upper troposphere and 700-750 m in the lower stratosphere. In order to  
140 convert the backscattered radiation profiles into water vapor mixing ratio profiles, the calibration coefficient is calculated  
141 from water vapor column ancillary data: GNSS (Global Navigation Satellite System) IWV (Integrated Water Vapor). The  
142 description of the calibration method and the total uncertainty budget can be found in Vérèmes et al. (2019).

143 At the Maïdo Observatory, the lidar provides 4 to 8 water vapor profiles per month. The calibrated lidar water vapor

144 database extends from November 2013 to December 2017. The time slot of routine operations is around 19:00 to 01:00 (+1)  
145 local time but there are intensive periods of observation during field campaigns that allow longer measuring span. The  
146 Raman lidar water vapor observations were validated during the Maïdo ObservatoRy Gaz and Aerosols NDACC Experiment  
147 (MORGANE) intercomparison exercise in May 2015 (Vérèmes et al., 2019). During the MORGANE campaign, CFH  
148 radiosonde and Raman lidar profiles showed mean differences smaller than 9 % up to 22 km asl.  
149 Here we used the Raman lidar measurements for two nights when the CFH sondes were launched at the Observatory (25  
150 January 2016 and 3 March 2017). The lidar water vapor profiles correspond to an integration time of 239 min and 184 min  
151 for the nights of 25 January 2016 and 3 March 2017 respectively. The lidar water vapor profiles are interpolated to the same  
152 200-m vertical grid used for the CFH data and are shown up to 14.5 km. The mean lidar uncertainties for the troposphere  
153 below this level are 10.5% and 8.7% for 25 January 2016 and 3 March 2017 respectively.

### 154 **2.3 Satellite data**

155 The brightness temperatures of the infrared (IR) channel at 10.8  $\mu\text{m}$  of the geostationary weather satellite METEOSAT-7  
156 have been used to provide the regional characteristics of deep convection over the Indian Ocean. The satellite centered at  
157 57.5°E provided images for the Indian Ocean from December 2005 to March 2017.

158 Aura Microwave Limb Sounder (MLS) v4.2 water vapor and ozone data were included in the study to compare with the in  
159 situ measurements and to evaluate the spatial extent of the convective air masses measured at the Observatory. In particular  
160 we have used water vapor from the Stratospheric Water and OzOne Satellite Homogenized (SWOOSH) data set (Davis et  
161 al., 2016). The SWOOSH dataset contains monthly mean stratospheric water vapor and ozone profiles from several satellite  
162 instruments for the period 1984 to present. The data are available on a 3D (longitude/latitude/pressure) grid. The SWOOSH  
163 input data for the period August 2004 to present day correspond to measurements from the Aura MLS satellite. The MLS  
164 water vapor data are available on a pressure grid with 12 levels per decade change in pressure between 1000 and 1 hPa (e.g.  
165 the vertical resolution is ranging from 1.3 to 3.6 km between 316 and 1 hPa). The estimated accuracy for MLS water vapor  
166 decreases from 20% at 216 hPa to 4% at 1 hPa and is  $\sim 10\%$  in the TTL region (150-70 hPa).

167 Cloud-Aerosol Lidar with Orthogonal Polarization (CALIOP) onboard Cloud Aerosol Lidar and Infrared Pathfinder Satellite  
168 Observation (CALIPSO) makes backscatter measurements at 532 nm and 1064 nm since June 2006. We use the Total  
169 Attenuated Backscatter coefficients  $\beta'_{532}$  available from the CALIPSO V4.10 level 1 lidar data products. Following Vaughan  
170 et al. (2004), the attenuated scattering ratio  $SR_{532}$  (Equation 3 of Vaughan et al., 2004) profiles are computed as the ratio of  
171  $\beta'_{532}$  corrected for molecular attenuation and ozone absorption and the molecular backscatter coefficient  $\beta_m$ .  $\beta_m$  is calculated  
172 using the number density of molecules from the GEOS 5 global model of the NASA Global Modeling and Assimilation

173 Office (GMAO) and the Rayleigh scattering cross section. More details are given in the CALIOP Algorithm Theoretical  
174 Basis Document (ATBD, cf. Equations 4.13a and 4.14).

## 175 **2.4 Model**

176 The origin of air masses measured at the Maïdo Observatory were assessed using the FLEXible PARTicle (FLEXPART)  
177 Lagrangian Particle Dispersion Model (Stohl et al., 2005). FLEXPART is a transport model that can be run either in forward  
178 or backward mode in time. FLEXPART was driven by using ECMWF analysis (at 00, 12 UTC) and their hourly forecast  
179 fields from the operational European Centre for Medium Range Weather Forecasts - Integrated Forecast System (ECMWF-  
180 IFS). In March 2016, ECMWF introduced a new model cycle of the IFS into operations with a grid-spacing of 9 km roughly  
181 doubling the previous grid-spacing of 16 km used since January 2010. The ECMWF model has 137 vertical model levels  
182 with a top at 0.01 hPa since June 2013. To compute the FLEXPART trajectories, the ECMWF meteorological fields were  
183 retrieved at 0.50° and 0.15° and on full model levels from the Meteorological Archival and Retrieval System (MARS) server  
184 at ECMWF. The 0.50° fields were used to drive the FLEXPART model over a large domain configured as a tropical  
185 channel, i.e., the domain is global in the zonal direction but bounded in the meridional direction (at latitudes  $\pm 50^\circ$ ).  
186 Furthermore, higher-resolution domains can be nested into a mother domain in a FLEXPART simulation. Thus, to have a  
187 better representation of convective transport associated with mesoscale convective systems or tropical cyclones with a  
188 horizontal dimension on the order of a couple of hundred kilometers over the SWIO, we included a nest domain covering the  
189 SWIO region (20°E-80°E, 40°S-10°N). If a particle resides in the high-resolution nest, the ECMWF meteorological data at  
190 0.15° from this nest are interpolated linearly to the particle position. If not, the 0.50x0.50° ECMWF meteorological data  
191 from the mother domain are used to compute the trajectories. Retrieving high-resolution ECMWF fields from the MARS  
192 server for FLEXPART consists in several steps which are:

- 193 - retrieve the meteorological model data output from ECMWF (horizontal winds, temperature, humidity, surface  
194 fields)
- 195 - compute total and convective precipitation rates, sensible and latent heat fluxes from the surface
- 196 - calculate the vertical velocity from the continuity equation

197 Therefore, the ECMWF high-resolution vertical velocity field already contains a convective mass flux component from the  
198 Tiedtke scheme used in ECMWF. The convective scheme used in the ECMWF-IFS, originally described in Tiedtke (1989),  
199 has evolved over time. Changes made include a modified entrainment formulation leading to an improved representation of  
200 tropical variability of convection (Bechtold et al. 2008) and a modified CAPE closure leading to a significantly improved  
201 diurnal cycle of convection (Bechtold et al. 2014). Particles are transported both by the resolved winds and parameterized

202 sub-grid motions, including a vertical deep convection scheme. FLEXPART uses the convective parameterization by  
203 Emanuel and Zivkovic-Rothman (1999) to simulate the vertical displacement of particles due to convection. The results from  
204 model runs with and without cumulus scheme in FLEXPART have been compared to assess whether convective mass fluxes  
205 could be resolved in the higher-resolution nest domain. The results of FLEXPART runs with and without cumulus scheme  
206 look fairly similar (not shown) and thus here we will present only the model results with cumulus scheme turned off.

207 To determine the transport history of air masses sampled by balloon launches, a so-called retroplume was calculated  
208 consisting of 10,000 back trajectory particles released from each 1 km layers of balloon launches used in this study, and  
209 advected backward in time. The initial positions of the 50,000 particles were distributed randomly within 19 vertical layers  
210 (corresponding to the MLS pressure levels between 316 and 10 hPa) with a depth of 1 km and  $0.10^{\circ} \times 0.10^{\circ}$  longitude-latitude  
211 bins centered on the balloon location. The dispersion of a retroplume backward in time indicates the likely source regions of  
212 the air masses sampled by the in situ instruments.

### 213 **3 Tropical storm Corentin (January 2016) and tropical cyclone Enawo (March 2017).**

#### 214 **3.1 Convective activity**

215 Figure 1 shows the best tracks (i.e. a smoothed representation of the tropical cyclone's location over its lifetime, red line on  
216 each panel of Figure 1) of Tropical Storm (TS) Corentin and Tropical Cyclone (TC) Enawo. The best track represents the  
217 best guess of the location of the tropical cyclone center every 6 hours. TS Corentin started to form on 19 January 2016, east  
218 of  $70^{\circ}\text{E}$ . The METEOSAT 7 IR brightness temperatures on 19 January 2016 at 11 UTC indicate a vast clockwise circulation  
219 with some organization (not shown), indicative of tropical cyclone formation in the SH. The strengthening of the northerly  
220 monsoon flow favored the deepening of the system in the subsequent days. Corentin became a moderate tropical storm (10-  
221 min maximum sustained wind speeds of 65 km/h) on 21 January 2016 at 00 UTC and at that time the TS center was located  
222 at  $14.93^{\circ}\text{S}$ ,  $75.63^{\circ}\text{E}$ ,  $\sim 2200$  km to the northeast of the island. TS Corentin continued to intensify on January 22 while  
223 moving towards the south (see best track on Figure 1). TS Corentin reached its peak intensity on January 23 at 00 UTC with  
224 10-minute maximum sustained wind speeds of 110 km/h and the pressure at the center was 975 hPa. On 23 January 2016,  
225 convection was strong around  $10^{\circ}\text{S}$  in the Mozambique Channel and near TS Corentin, especially in the northern part of the  
226 system. On January 24, Corentin had weakened into a moderate tropical storm. On 25 January at 18 UTC (time of the  
227 balloon launch at the Maïdo Observatory), the storm was located at about 2500 km southeast of Réunion Island, near  $26.03^{\circ}$   
228 south latitude and  $79.19^{\circ}$  east longitude (Figure 1).

229 The Madden Julian Oscillation (MJO) was active at the end of February and during the first week of March 2017 with a



230 signal centered over Africa and the Indian Ocean. A monsoon trough was well defined all over the basin along 9°S. On 28  
231 February 2017 at 10 UTC, a zone of disturbed weather formed around 6.5°S, 70.2°E (not shown) with the building of  
232 clockwise rotating movement inside the cloud pattern. Favored by the MJO active phase and the arrival of an equatorial  
233 Rossby wave, Enawo initially formed as a tropical disturbance on March 2 with 10-minute maximum sustained wind speeds  
234 ~ 40 km/h. Enawo intensified to a moderate tropical storm at 06:00 UTC on March 3. At the time of the balloon launch at the  
235 Observatory (~3 March, 18 UTC), Enawo was a tropical storm located near 13° south latitude and 56.42° east longitude,  
236 about 900 km north-northwest of Réunion Island (Figure 1). It strengthened into a severe tropical storm cyclone on 5 March  
237 at 00 UTC and became a category 1 tropical cyclone at 12 UTC. TC Enawo continued to intensify while moving toward  
238 Madagascar. It became a category 4 tropical cyclone on March 6 at 18:00 UTC, with 10-minute maximum sustained winds  
239 at 194 km/h. Enawo reached its peak intensity at 06:00 UTC on March 7, with ten-minute maximum sustained winds at 204  
240 km/h and the central pressure at 932 hPa. TC Enawo reached Madagascar's northeastern coast on March 7 at around 9:30  
241 UTC and was the third strongest tropical cyclone on record to strike the island. After March 8, TC Enawo gradually  
242 weakened to a tropical storm while moving southward over Madagascar.

243 The two balloon launches at the Observatory on 25 January 2016 and 3 March 2017 were specifically planned using  
244 FLEXPART Lagrangian trajectories and METEOSAT 7 infrared images. The goal was to sample the convective outflow  
245 from TS Corentin and TC Enawo as well as convection north of Madagascar on 24 January 2016.

246 To assess the potential effects of deep convection in the upper troposphere and near the tropopause, we looked at the  
247 distribution of deep convective clouds in the days preceding the soundings. The location of deep convective clouds can be  
248 assessed by using maps of METEOSAT 7 infrared brightness temperature. Figure 2 shows convective cloud coverage for the  
249 3-day period preceding the sonde launch date at the Maïdo Observatory. Convective cloud coverage was estimated using 3-  
250 hourly METEOSAT 7 infrared brightness temperatures at 5 km resolution. A threshold of 230 K is used to detect deep  
251 convective clouds in the METEOSAT 7 brightness temperature data (i.e. pixels with brightness temperatures less than 230 K  
252 correspond to convective clouds). This threshold has been previously used to identify convection on geostationary satellite  
253 infrared images (e.g. Tissier et al., 2016). This temperature corresponds to a height of about 11 km in the NDACC/SHADOZ  
254 climatological-mean summertime profile of temperature. Prior to 25 January 2016, the main deep convective activity is  
255 located ~1500 km north of the island between 50 and 70°E and around tropical storm Corentin. From 28 February to 3  
256 March 2017, convective clouds are located ~500 km north of the island and correspond to the intensifying tropical storm  
257 Enawo. The coldest cloud tops ( $\leq 190$  K) that correspond to the deepest convection are indicated by red dots on Figure 8.

### 258 **3.2 Monthly mean water vapor distributions.**

259 Figures 3 show MLS water vapor volume mixing ratios at 215 hPa and 100 hPa averaged over January 2016 and March  
260 2017. These values were computed by averaging the SWOOSH monthly mean water vapor concentrations gridded on a  
261 regular pressure/latitude/longitude (resolution of 5°X20°) grid.

262 When comparing the water vapor mixing ratio at 215 hPa in January 2016 to the one observed in March 2017, one can see  
263 that the upper troposphere over the SWIO was much moister in January 2016 than in March 2017 with three distinct regions  
264 of enhanced water vapor over Central Africa, the Indian Ocean and the Maritime Continent. The mean water vapor mixing  
265 ratio at 215 hPa over the SWIO in January 2016 is greater by ~23 ppmv compared to March 2017. Interannual variability  
266 modes such as the El-Niño–Southern Oscillation (ENSO) can affect the TTL temperature, and thus, water vapor distribution.  
267 The NOAA Climate Prediction Center Ocean Niño index (ONI), which is based on SST anomalies in the Niño 3.4 region,  
268 was equal to +2.5 K in January 2016 versus +0.1 K in March 2017  
269 ([http://origin.cpc.ncep.noaa.gov/products/analysis\\_monitoring/ensostuff/ONI\\_v5.php](http://origin.cpc.ncep.noaa.gov/products/analysis_monitoring/ensostuff/ONI_v5.php)). January 2016 corresponded to strong  
270 El Niño conditions (one of the strongest El Niño event since 1950 according to the ONI index) while March 2017 was  
271 associated with neutral ENSO conditions. The water vapor mixing ratios at 215 hPa for January 2016 are in agreement with  
272 MLS DJFM climatological values of water vapor at 215 hPa for El Niño conditions (not shown). Overall during El Niño  
273 conditions, water vapor mixing ratios at 215 hPa are enhanced over the SWIO west of 80°E. Ho et al. (2006) have studied  
274 the variations of TC activity in the South Indian Ocean in relation to ENSO effects. During El Niño periods TC genesis was  
275 shifted westward, enhancing the formation west of 75°E and reducing it east of 75°E. Therefore, on January 2016 the peak of  
276 water vapor west of 80°E at 215 hPa may be related to an increase in convection associated with strong El Niño conditions.

277 The Quasi-Biennial Oscillation (QBO) also affects TTL temperatures and humidity (e.g. Zhou et al., 2001; Yuan et al., 2014;  
278 Davis et al., 2013). Following Davis et al. (2013), we defined a QBO index as the zonal mean (10°S-10°N) of the difference  
279 in the ERA-Interim zonal wind at 70 and 100 hPa. A positive QBO index ( $u_{70\text{hPa}} - u_{100\text{hPa}} > 0$ ) corresponds to westerly shear  
280 conditions and the warm phase of the QBO (Baldwin et al., 2001). A negative QBO index corresponds to easterly shear  
281 conditions and the cold phase of the QBO (CPT temperatures are cooler during the easterly shear phase of the QBO). The  
282 mean January 2016 water vapor mixing ratio at 100 hPa over the SWIO is 4.2 ppmv versus 3.7 ppmv in March 2017 as  
283 compared to the climatological values of 3.51 ppmv for January and 3.44 ppmv of March. The difference of 0.50 ppmv  
284 between the two periods cannot be explained by the phase of the QBO as both months corresponded to QBO westerly shear  
285 conditions (2.33 m/s for January 2016 and 4.79 m/s for March 2017). However, the higher water vapor mixing ratio at 100  
286 hPa in January 2016 could be related to strong El Niño conditions as Avery et al. (2017) have reported large lower  
287 stratospheric (82 hPa) water vapor anomalies (~ +0.9 ppmv) associated with the strong 2015-2016 El Niño. The highest  
288 SWOOSH water vapor mixing ratio anomalies of ~ +1 ppmv were observed over the Indian Ocean in December 2015 (not  
289 shown). In January 2016, the anomalies over the SWIO have eased to 0.7 ppmv (not shown).

290

## 291 **4. Observations**

### 292 **4.1 Water vapor/ozone profiles**

293 Figure 4 shows two CFH water vapour mixing-ratio profiles (black lines) taken at the Maïdo Observatory on 25 January  
294 2016 at 17:50 UTC and 3 March 2017 at 18:00 UTC. The lidar water vapor profiles for those two nights are also displayed in  
295 green. The red and purple lines correspond to NDACC/SHADOZ ozonesonde balloon profiles launched from Gillot on 18  
296 January 2016 (purple line), 4 February 2016 (red line) and 3 March 2017 (purple line on the right panel). The ozonesonde  
297 data correspond to daytime measurements (balloon launches at ~11 UTC) while the CFH water vapor data correspond to  
298 nighttime measurements in order to coincide with water vapor lidar measurements at the Maïdo Observatory. Overall good  
299 agreement is seen between the lidar and CFH water vapor profiles over the whole troposphere. Note that the CFH water  
300 vapor profiles were not used to calibrate the lidar water vapor profiles as explained in section 2.2.

301 The altitude range 2-12 km on 25 January 2016 is moister by ~50% than the same altitude range on 3 March 2017 (mean  
302 water vapor mixing ratio of 5076 ppmv and 4375 ppmv between 2 and 12 km on 25 January 2016 for the CFH and lidar  
303 respectively versus 3335 ppmv and 3398 ppmv on 3 March 2017 for the CFH and lidar respectively). The austral summer  
304 season, with warmer temperatures and greater cloudiness, reaches its peak in January/February and this could explain in part  
305 the higher humidity observed in January than March. In addition, January 2016 corresponded to a strong El Niño period and  
306 this could lead to higher tropospheric moistening associated with ENSO (Tian et al., 2019). On 3 March 2017, a moist layer  
307 was observed between ~12 and 16 km in both CFH and lidar water vapor profiles with corresponding low ozone values  
308 (Figure 4, right). On 25 January 2016, two local moist layers around 10 and 15 km associated with low ozone are observed.  
309 The lidar smooths out the peak of water vapor at 10 km observed on 25 January 2016 but this could be due to the longer  
310 integration time used for that night (239 min). The CFH water vapor mixing ratio profiles have a minimum of 2.5 ppmv at  
311 17.10 km (94 hPa) and 2.70 ppmv at 18.10 km (77.1 hPa) on 25 January 2016 and 3 March 2017 respectively.

312 Also shown is the climatological mean ozone profile for DJFM 1998-2017 (blue lines on Figure 4). Anomalously low  
313 mixing ratios approaching surface values are seen in the upper troposphere for both the 4 February 2016 (red line, Fig. 4a)  
314 and 3 March 2017 (purple line, Fig. 4b) ozone sonde flights. In the upper troposphere, the climatological mean ozone mixing  
315 ratios ranges from about 60 ppbv at 10 km to 100 ppbv at 15 km. There is a steep gradient above 17 km, indicating the  
316 transition from troposphere to stratosphere. On 3 March 2017, ozone mixing ratios between 10 and 15 km are ~ 45 ppbv  
317 below the climatological values (mean value of 25.10 ppbv for the 10-15 km layer on 3 March 2017 versus 70.1 ppbv for the  
318 climatological ozone profile).

21  
22

319 Between 18 January and 4 February 2016, ozone mixing ratios in the upper troposphere decreased by  $\sim 30$  ppbv and are 38  
320 ppbv below the climatological values on 4 February 2016. Tropical storm Corentin reached its peak intensity on 23 January  
321 2016 at 00 UTC and its center was located 1735 km east of Réunion Island. These low ozone mixing ratios in the upper  
322 troposphere on 4 February 2016 were observed after the storm had its major influence on UT ozone, transporting air with  
323 surface ozone values upward via strong convection and mixing out into the larger environment. In comparison, the 18  
324 January 2016 ozone profile was not influenced by TS Corentin. The lower ozone values on 3 March 2017 compared to those  
325 observed on 4 February 2016 could be explained by the fact that TC Enawo was closer to the island ( $\sim 902$  km north of the  
326 island), was still intensifying and was a stronger system than TS Corentin. Above  $\sim 17$  km the ozone profiles in  
327 January/February 2016 and March 2017 are more similar to the climatological mean ozone profile, suggesting that deep  
328 convection did influence the upper troposphere but not the lower stratosphere. We will later show using FLEXPART that the  
329 moist/low ozone layers in Figure 5 are associated with the convective outflow of a mesoscale convective system north of  
330 Madagascar on 23 January 2016, TS Corentin and TC Enawo.

#### 331 **4.2 Relative humidity and temperature profiles**

332 Figure 5 shows the CFH profiles of  $RH_{ice}$  (computed using the Goff-Gratch equation [Goff and Gratch, 1946] for water vapor  
333 pressure) on 25 January 2016 and 3 March 2017 as well as collocated CALIOP nighttime backscatter measurements. The  
334 CALIOP measurements shown on Figure 5 include only those within  $\pm 5^\circ$  latitude and  $\pm 10^\circ$  longitude of the Maïdo  
335 Observatory. The CALIOP measurements on 25 January 2016 correspond to a CALIPSO overpass east of the island around  
336 4 hours after the balloon launch and the mean longitude difference between the CALIPSO overpass and the Maïdo  
337 Observatory is  $2.4^\circ$  for Figure 5-top. On 3 March 2017, the CALIPSO overpass was west of the island and also 4 hours after  
338 the balloon launch. The mean longitude difference between the CALIPSO overpass and the Maïdo Observatory is  $5.3^\circ$ . The  
339 latitude-height cross-section of CALIOP  $SR_{532}$  on Figure 5 corresponds to measurements with a 60 m vertical resolution. The  
340 horizontal interval of the CALIOP data along its orbit is 330 m; for this study we use a 9-point running average to reduce  
341 noise.

342 Figure 5 (top) shows significant structure in the  $RH_{ice}$  profile measured on 25 January 2016. Higher values of  $RH_{ice}$  ( $> 40\%$ )  
343 between 13 and 15 km coincide with higher values of CALIOP  $SR_{532}$  between 12 and 15 km. The  $RH_{ice}$  reaches its maximum  
344 value at the coldpoint altitude (17.3 km). The CALIOP  $SR_{532}$  indicates a cirrus cloud between  $\sim 12$  and 15 km north of the  
345 island. The cirrus layer extends from  $\sim 16.2^\circ S$  to  $20^\circ S$  corresponding to a horizontal scale of  $\sim 400$  km. METEOSAT 7  
346 infrared brightness temperature at 21:30 UTC, so  $\sim 10$  minutes before the CALIPSO overpass at 21:39 UTC on Figure 5  
347 (top), indicates a large area of deep convection near  $15^\circ S$  and extending from  $\sim 50^\circ$  to  $75^\circ E$  (not shown). The monsoon  
348 trough was located between  $17^\circ S/50^\circ E$  and  $14^\circ S/70^\circ E$  on 25 January 2016 which promoted deep convection and convective

349 activity was also observed in the South-Eastern quadrant of TS Corentin. The cirrus cloud observed below 15 km on Figure  
350 5 (top) was most likely from convective detrainment north of Réunion Island. The  $RH_{ice}$  profile on January 25 indicates  
351 intertwined layers of dry air ( $RH_{ice}$  less than 40%) at 7, 9, 12 and 16 km and less dry air ( $RH_{ice} \sim 50\%$ ) at 8, 11, 15 and 17km.  
352 While convection north of Réunion Island around 15°S and TS Corentin had mixed the troposphere over the Southwest  
353 Indian Ocean, no cirrus clouds were directly observed on 25 January 2016 above the Maïdo Observatory. The layers of  $RH_{ice}$   
354  $\sim 50\%$  at 15 and 17 km may be due to convective detrainment. The cirrus cloud below 15 km detected by CALIPSO north of  
355 the island on January 25 indicates that deep convection detrained ice and water vapor in the upper troposphere north of the  
356 island. There was a northerly wind between 10 and 17 km on 25 January 2016 with a peak around  $-25 \text{ m s}^{-1}$  at 15 km (cf.  
357 Figure 1). Moist air detrained by deep convection north of Réunion near 15°S may have been transported to Réunion Island  
358 in  $\sim 6$  hours and during that time the moist air mass could have mixed with drier air, thereby explaining the layers of  $RH_{ice} \sim$   
359  $50\%$  at 15 and 17 km on Figure 5. The origin of these layers has also been determined using the FLEXPART Lagrangian  
360 model, and the results are presented in the next section.

361 On 3 March 2017, a layer close to saturation ( $RH_{ice} > 80\%$ ) can be observed between 12 and 16 km (Figure 5, bottom left)  
362 with  $RH_{ice}$  up to  $\sim 100\%$  at 12.5 and 14 km, below the coldpoint altitude (16.1 km). The altitude range 12-15.5 corresponds  
363 to cloudy air and a cirrus cloud can be seen in the CALIOP measurements of  $SR_{532}$  between  $\sim 13$  and 15 km extending from  
364 18.4°S to 21.2°S (Fig 6, bottom right). Above Réunion Island, the cirrus is  $\sim 1.5$ km thick and the maximum thickness of  $\sim 3$   
365 km is observed north of the island at 20.5°S. A second cirrus cloud can also be observed below 15 km north of 17.4°S.

366 The CPT height is 16.10 km on 3 March 2017 while it is 1.2 km higher on 25 January 2016 (Figure 5). The CPT temperature  
367 was 192.64 K on 25 January 2016 and 194.58 K on 3 March 2017. On 3 March 2017, the layer between 16 and 18 km is  
368 almost isothermal with a mean temperature of 195 K while the tropopause is sharper on 25 January 2016.

### 369 **4.3 Lagrangian analysis**

370 The convective origin of air masses sampled in the upper troposphere and near the tropopause during the passage of TS  
371 Corentin and TC Enawo is evaluated using the FLEXPART Lagrangian model. Figure 6 presents the origins of air masses  
372 sampled within layer L1 (12.1-13.1km,  $\sim 178$ hPa) and layer L2 (16.3-17.3km,  $\sim 100$ hPa), altitudes that correspond to RHi  
373 peaks on Figure 5 on January 25 2016 above the Maïdo Observatory. The origins and pathways of these air masses were  
374 examined by computing 10-day FLEXPART back trajectories. On Figure 6, the origins of air masses measured in the upper  
375 troposphere (layer L1) and near the tropopause (layer L2) are shown for two day and three days prior to the launch. The  
376 position of each air mass is depicted by 10,000 dots color coded by their altitude and is overlaid over METEOSAT 7 infrared  
377 images valid at the time of the back trajectories. For example, trajectories that were originally in the lower troposphere

378 (below 5 km) and middle troposphere (between 5 and 10 km) two/three days before are indicated by orange and brown dots  
379 respectively. In other words, these air masses were transported from the troposphere to the upper-troposphere/tropopause  
380 region in two or three days before being sampled by the CFH instrument on 25 January 2016 around 18:30 UTC above the  
381 Maïdo Observatory. The air mass fractions for different altitude ranges are also indicated at the bottom of Figure 6.  
382 Variations in the air mass fractions over time (e.g. from the lower troposphere below 5 km) can be interpreted in terms of  
383 changes in the vertical transport due to convection over the SWIO.

384 The ability of FLEXPART to represent isolated deep convective cells is limited, due to the  $0.15^{\circ} \times 0.15^{\circ}$  spatial resolution of  
385 the ECMWF operational fields. At that resolution, isolated deep convective cells are not fully resolved in the ECMWF  
386 vertical wind field, and their updraft intensity and the altitude of the level of neutral buoyancy could be underestimated.  
387 However, the vertical transport of convective cells organised at mesoscale such as convection in tropical cyclones that cover  
388 several degrees in longitude and latitude are better resolved by the  $0.15^{\circ} \times 0.15^{\circ}$  ECMWF meteorological fields. Recent  
389 improvements of the ECMWF IFS model have enhanced its forecasting skills of tropical cyclones (Magnusson et al., 2019).  
390 Hence the FLEXPART backtrajectories driven by the ECMWF operational wind field give a qualitative sense of convective  
391 origins of vertical layers measured at Maïdo in relation to tropical cyclones.

392 According to FLEXPART, layer L1 measured above the Maïdo Observatory on 25 January 2016 ~18:30 UTC has two  
393 different origins. Two days before (Figure 6, top left), 48% of this air mass was below 10 km (with ~31% below 5 km) and  
394 ~1000 km northeast of Réunion Island in a region with convective clouds with cold brightness temperatures less than 220 K  
395 (~12 km). Therefore, we can infer that the majority of the layer L1 was lifted by convection associated with TS Coentín two  
396 days prior to the launch. These trajectories are rather spread in the lower troposphere, suggesting that they experienced  
397 turbulent mixing and changes in wind direction in the lower troposphere. The rest of the trajectories are located higher in  
398 altitude, in the 10-15 and 15-17 km altitude ranges. They are also located above convective clouds but are less scattered than  
399 the trajectories in the lower troposphere, suggesting that these trajectories were less mixed with the surrounding upper  
400 troposphere.

401 Three days before (Figure 6, top right), 66% of layer L1 originated from the lower and middle troposphere (41% within the  
402 0-5 km layer, 25% within the 5-10 km layer) over the northeastern convective region of TS Coentín, and 32% from the  
403 upper troposphere (within 10-15 km) above TS Coentín. The upper tropospheric branch had an anticlockwise rotation with  
404 an origin near TS Coentín, in agreement with the upper divergence associated with TS Coentín. Hence, most of the air  
405 mass was located either in the lower troposphere or near the top of convective clouds three days before.

406 Layer L2 measured at Maïdo on 25 January 2016 stayed in the upper troposphere and near the tropopause two days before

407 reaching Réunion Island (figure 6, bottom left). The trajectories followed an anticlockwise rotation associated with  
408 Corentin's dynamics and were located ~250 km north of the center of TS Corentin. Only 3% of trajectories that originate in  
409 the lower troposphere were found. On 22 January at 17 UTC (three days before the launch), the trajectories were located  
410 East of the center of Corentin (Figure 6, bottom right). About 8% of the trajectories were below 10km (6.4% below 5km).  
411 Note that TS Corentin reached its peak intensity on 23 January 2016 at 06 UTC (pressure at the center of 975 hPa, ten-  
412 minute maximum sustained winds of 110 km/h). Hence, according to FLEXPART backtrajectories and the METEOSAT 7  
413 infrared images, the origin of layer L2 was traced back to the active convective regions of TS Corentin and its upper  
414 divergence dynamics, but a small fraction originated from the lower troposphere. However, due to the 0.15° spatial  
415 resolution of the ECMWF winds used to drive FLEXPART, the vertical updrafts of the deepest convective clouds that may  
416 reach the tropopause region/lower stratosphere may not be well represented in FLEXPART.

417 Figure 7 is similar to Figure 6 but for backtrajectories associated with the launch on 3 March 2017. Most of the layer L4  
418 measured on 3 March 2017 at 18:42UTC was lifted by convection 800 km north of the island two to three days before  
419 (Figure 7 top). Two days before (Figure 7, top left), the backtrajectories indicate that a large fraction (69%) of layer L4 is  
420 from the lower troposphere (below 10 km) over a convective region associated with TC Enawo. Three days before reaching  
421 Réunion Island (Figure 7 top right), the trajectories were dispersed in the lower troposphere around the forming storm as  
422 Enawo was in the early stage of its formation at that time (tropical depression).

423 The FLEXPART backtrajectories for layer L5 measured above the Maïdo Observatory on 3 March 2017 at 18:52 UTC  
424 stayed in the upper troposphere two and three days before the launch (Figure 7 bottom). The trajectories were confined to the  
425 same latitude band east and west of Réunion Island in a clear sky region, away from convective clouds. It shows that air  
426 masses near the tropopause above Réunion Island on 3 March 2017 were most likely not affected by Enawo at this stage of  
427 its development as Enawo was still intensifying.

428 In a nutshell, the FLEXPART backtrajectories clearly identify a convective origin for layers L1 and L4 sampled on 25  
429 January 2016 and 3 March 2017 associated with TS Corentin and TC Enawo tropical cyclones. The convective transport  
430 from the lower troposphere to the upper troposphere occurred roughly two days before each launch. As for the tropopause  
431 region over Réunion Island on 25 January 2016, FLEXPART backtrajectories suggest that the air masses were embedded in  
432 TS Corentin upper divergence dynamics over a region where convection was active. Deep convective clouds within TS  
433 Corentin may have reached the tropopause region (layer L2) on 23 January 2016 when the storm was at its peak intensity  
434 and may have influenced the water vapor content near the tropopause. On 3 March 2017, the tropopause region measured by  
435 the CFH sounding was not affected by deep convection associated with Enawo according to the model, at least not at the  
436 time of the observation. At that time, TC Enawo was still intensifying and the deepest convective cloud developed later after

437 4 March 2017.

438

## 439 **5. Discussion**

### 440 **5.1 CFH and MLS comparisons**

441 The CFH measurements analyzed in this study are compared to coincident MLS profiles. The match criteria used are  $\pm 18$ h,  
442  $\pm 500$  km North-South distance (around  $\pm 5^\circ$  latitude),  $\pm 1000$  km East-West distance (around  $\pm 10^\circ$  longitude). The same  
443 match criteria are used in Davis et al. (2016). In addition, FLEXPART backtrajectories initialized at each MLS pressure  
444 levels are used to isolate the MLS profiles that were originating from TS Corentin and TC Enawo. 5 and 3 matched MLS  
445 profiles are found for 25 January 2016 and 3 March 2017 respectively. On 25 January 2016, distances between the Maïdo  
446 Observatory and the matched MLS profiles range from 259 to 494 km, with a mean distance of 346 km. The mean time  
447 difference for all matched profiles is 3.7 h. On 3 March 2017, the 3 matched MLS profiles are closer to the Maïdo  
448 Observatory with a mean distance of 281 km and are east of the island. However, a larger mean time difference of 16.4 h is  
449 observed for the matched MLS profiles.

450 To compare the high-resolution CFH water vapor profile to the MLS satellite data, we smooth the high resolution sonde  
451 measurements to match the resolution of the satellite profiles using the MLS vertical averaging kernels, following the  
452 procedure described in Read et al. (2007) and Davis et al. (2016). The procedure for applying the MLS averaging kernels to  
453 a CFH profile requires an a priori profile as input; this is the same a priori profile used in the MLS retrieval. Figure 8 shows  
454 the matched MLS profiles and the CFH profiles convolved with the MLS averaging kernels. The matched MLS profiles on  
455 both dates illustrate how water vapor is more variable in the upper troposphere (between 316 and  $\sim 147$  hPa) compared to  
456 above. The lower part of the tropopause layer from 147 hPa to the cold point tropopause (green dashed line on Figure 8) is a  
457 transition region where water vapor mixing ratios become lower but could still be influenced by deep convective outflow.  
458 The application of the averaging kernel to the CFH profiles smoothes the fine-scale structures observed in the CFH profiles  
459 on Figure 4 but still captures the deep layers of moist air in the upper troposphere between 261 and 147 hPa. To facilitate  
460 the comparison of CFH and MLS water vapor profiles in the upper troposphere and stratosphere where water vapor mixing  
461 ratios decrease by 3 orders of magnitude, we compute a mean percent difference of the MLS collocated profiles to the CFH  
462 and MLS data (i.e., percent difference =  $(\text{MLS} - \text{CFH}) / ((\text{CFH} + \text{MLS}) / 2) \times 100$ ). The same definition is used in Davis et al.  
463 (2016) and ensures that the distribution of percent difference at each pressure level is not skewed toward positive values  
464 larger than 100% (since water vapor values are constrained to be positive). In addition, this facilitates comparison with the  
465 study of Davis et al. (2016) that established a comparison between the 2004-2015 MLS water vapor data record and both



466 routine monitoring and field campaign frost point hygrometer balloon soundings at various stations around the world.

467 ~~The mean percent difference between the collocated MLS profiles and CFH convolved profile is shown on the right panel of~~  
468 ~~Figure 8. In the upper troposphere (layers L1, L2 and L4), MLS profiles tend to be wetter than the CFH measurements by~~  
469 ~~9±22% on 25 January 2016 and drier by 28±32% on 3 March 2017.~~

470 Several factors could explain why a dry bias exists between the mean MLS profile and CFH convolved profile on 3 March  
471 2017. First, the 3-km deep wet layer observed on March 2017 in the CFH profile will not be well captured by MLS with a 2-  
472 3 km vertical resolution in the upper troposphere. In addition, the CFH launch on 3 March 2017 at 18 UTC was planned  
473 using FLEXPART Lagrangian trajectory analysis and satellite images in the days prior to the launch to sample the  
474 convective detrainment of TC Enawo. Therefore, the planning of the CFH launch on 3 March 2017 was optimal to sample  
475 moist air from convective detrainment and an average of 3 MLS coincident profiles over a larger region/time window could  
476 be an underestimate of the storm related moistening. It is also known that the stirring of air masses due to tropical cyclones  
477 generates a rather inhomogeneous atmospheric composition up to the TTL (Cairo et al., 2008 and references therein). It is  
478 possible that the CFH on 3 March 2017 sampled a fresher tropospheric filament with higher humidity than the 3 MLS  
479 profiles.

480

481 On 25 January 2016, the mean MLS water vapor profile agrees well with the convolved CFH profile over the entire lower  
482 tropical stratosphere within layer L3. The mean percent difference is  $+7 \pm 10\%$  ( $+0.3$  ppmv) and lies within the previously  
483 published uncertainty of both instrument (Hurst et al., 2014; Vömel et al., 2007a; Davis et al., 2016; Yan et al., 2016).

484 On 3 March 2017, larger differences of  $+18\%$  ( $\sim 0.6$  ppmv) are observed in the lower stratosphere, between 121 and 32 hPa.  
485 It is not clear why there are larger differences in the stratosphere on 3 March 2017. Both CFH instruments launched on 25  
486 January 25 2016 and 3 March 2017 were prepared by the same operator and calibrated using the same recommended  
487 procedure. During these two flights, the CFH data streams were transmitted to receiving equipment on the ground through  
488 the Internet radiosonde. From an instrumental standpoint, there is nothing that might explain a CFH dry bias on 3 March  
489 2017 compared to 25 January 2016. Unfortunately, the CFH sondes are not recovered on the island after each flight as they  
490 land in the ocean and thus it was not possible to examine in more details the instrument after the flight on 3 March 2017. To  
491 our knowledge, the CFH instrument on that night has measured as well as it could in the stratosphere. Even though the CFH  
492 instrument launched on 3 March 2017 had a dry bias of 1 ppmv in the stratosphere, such bias does not affect the results of  
493 this paper found for TC Enawo.

494 Overall, the MLS mean profile agrees within uncertainty range with the CFH profile on 25 January 2016. On 3 March 2017,  
495 the MLS mean profile is drier than CFH in the upper troposphere, probably due to a lack of vertical resolution in MLS, and  
496 inhomogeneity in the atmospheric composition.

## 497 **5.2 Temperature anomaly**

498 The hypothesis of a potential influence of convection on the CFH water vapor profile is further tested by analysing the  
499 profile of temperature anomaly. A seasonal mean (December-March) temperature profile is computed for the period 1997-  
500 2017 using the NDACC/SHADOZ dataset. The weekly NDACC/SHADOZ launch is performed at the airport in the north  
501 part of the island (Gillot, 20 m a.s.l.). The flying distance between the Maïdo Observatory and the airport is ~20 km so while  
502 boundary layer temperature values will differ for the two sites, free troposphere/TTL temperature distributions can be  
503 compared as they are less influenced by topography. The seasonal mean CPT height is 17.31 km for the period December-  
504 March with a mean CPT temperature of 193.90 K (Table 1). The tropical tropopause is higher and colder during austral  
505 summer as a response to large-scale upwelling in the tropical stratosphere (Yulaeva et al., 1994) and convection (Highwood  
506 and Hoskins 1998). The iMet radiosonde temperature profiles are then compared to the seasonal mean NDACC/SHADOZ  
507 temperature profile. The upper panels on Figure 5 show temperature profiles from NDACC/SHADOZ and the iMet  
508 radiosonde. The black line shows the NDACC/SHADOZ seasonal mean temperature profile while the red line corresponds  
509 to the iMet temperature profile observed at the Maïdo Observatory.

510 A large positive temperature anomaly is observed on 25 January 2016 over a broad tropospheric region from 2 to 16 km  
511 (mean amplitude of +2.5 K) with a peak warming of +4.6 K at 10km (Figure 5, magenta line). On 3 March 2017, a warm  
512 temperature anomaly is mostly observed between 6 and 14 km (mean amplitude of +1.1 K) with a peak value of +3.1 K near  
513 12 km. The stronger warming of the troposphere observed in January 2016 may be due to the strong 2015/2016 El Niño. The  
514 connection between interannual variations in tropical tropospheric temperature and ENSO is well established (e.g., Yulaeva  
515 and Wallace 1994; Soden 2000). Using 13-year of temperature data from the tropospheric channel of the microwave  
516 sounding unit (MSU-2), Yulaeva and Wallace (1994) showed that a tropospheric warming occurs almost uniformly over the  
517 tropics and that the magnitude of the warming is around 0.5-1°C for strong El Niño years. Chiang and Sobel (2002) updated  
518 the analysis of Yulaeva and Wallace to include the response to the strong 1997/98 El Niño (ONI of +2.2 K in DJF 1998) and  
519 indicated MSU-2 temperature anomaly of ~1.2 K in January 1998 (cf. Figure 1 of Chiang and Sobel, 2002). Note that the  
520 MSU-2 temperature data used in these studies provide a measure of the mean temperature of the 1000-200 mb layer  
521 (corresponding to the surface to ~ 11 km using a scale height of 7 km). Thus, part of the strong tropospheric warming  
522 (especially in the lower part of the troposphere) observed in January 2016 may be due to the strong 2015/2016 El Niño (ONI  
523 of +2.5 K in DJF 2016). Assuming a tropospheric warming of ~ 1K in response to a strong El Niño, the magnitude of the

524 upper tropospheric warming observed on 25 January 2016 (mean amplitude of 3.4 K between 10 and 14 km) becomes more  
525 similar to the one observed on 3 March 2017 (mean amplitude of 1.9 K between 10 and 14 km) if the effect of the 2015/2016  
526 El Niño is removed.

527 Figure 5 indicates cold temperature anomalies within 16-19 km above the tropospheric warm anomalies on 25 January 2016.  
528 The mean amplitude of the 16-19 km temperature anomaly is -1.6 K with a maximum cooling of -3.6 K at 18 km. A similar  
529 feature is observed on 3 March 2017, with a cooling between 14 and 17 km with a mean amplitude of -2 K and maximum  
530 cooling of -4.5 K at 15.1 km. The upper tropospheric warming and near tropopause cooling observed on both dates is  
531 consistent with a temperature response to deep convection (e.g. Sherwood et al., 2003; Holloway and Neelin, 2007; Paulik  
532 and Birner, 2012). The cooling around the tropopause can be explained by either radiative cooling by cirrus clouds over the  
533 regions of deep convection (Hartmann et al., 2001) or diabatic cooling through convective detrainment (Sherwood et al.,  
534 2003; Kuang and Bretherton, 2004). CPT properties can also be modified by convectively driven waves (Zhou and Holton,  
535 2002; Randel et al., 2003).

536 Paulik and Birner (2012) investigated the deep convective temperature signal based on SHADOZ ozone and temperature  
537 data. Low ozone concentrations in the upper troposphere are indicative of convective transport from the boundary layer.  
538 They looked at temperature anomalies corresponding to low ozone anomalies between 12 and 18 km, thus temperature  
539 anomalies influenced by deep convection. A strong warming was observed near the level of main convective outflow at ~12  
540 km and cooling was more pronounced above ~ 15 km and near the CPT at ~17 km. Thus, the upper tropospheric warm  
541 temperature anomalies as well as cold temperature above 15 km and near the tropopause on Figure 5 are coherent with a  
542 deep convective temperature signal. Paulik and Birner's study also showed that the amplitude of the temperature anomalies  
543 increases as convection strengthens with a warming of ~2K in the upper troposphere and a cooling of around -3K near 16 km  
544 (cf. Figure 5 of Paulik and Birner, 2012). Using CloudSat observations of deep convective clouds and COSMIC GPS  
545 temperature profiles, they showed that the deep convective temperature signal (i.e. anomalously warm upper troposphere and  
546 an anomalously cold upper TTL) was only present for deep convective clouds above 15 km. Although the magnitude of the  
547 temperature anomalies decreases with increasing distance from convection, they observed a deep convective temperature  
548 signal during DJF ~3500 km away from the convective event. Within 1000 km of the deepest convection (deep convective  
549 clouds above 17 km), the convective temperature anomaly exceeds 0.75 K in the upper troposphere and ranges from -1 K to  
550 -2.0 K near 16 km. In our case, the deepest convective clouds with cloud tops colder than 190 K are 1000 km away from the  
551 island on 22-25 January 2016 and are closer from the island at ~500 km on 28 February-3 March 2017 (Figure 2). Although  
552 deep convective clouds observed on 22-25 January 2016 and 28 February-3 March 2017 were not in the immediate vicinity,  
553 relatively fast-moving gravity waves caused by deep convection could spread the deep convective temperature signals over  
554 large regions in short amounts of time (Holloway and Neelin, 2007). The temperature anomalies in Figure 5 are much larger

555 than those reported by Paulik and Birner for temperature profiles around the time ( $\pm 6$  hours) and location of deep  
556 convection (within 1000 km). However, we are studying deep convective temperature anomalies associated with two  
557 individual events while their deep convective temperature signal was estimated using 4 years of COSMIC data. Therefore,  
558 their estimates correspond to an average deep convective temperature signal; such a signal is likely larger when considering  
559 larger/more organized convective events such as tropical storms.

560 Hence, the temperature anomalies derived from the 25 January 2016 and 3 March 2017 profiles are coherent with a deep  
561 convective outflow in the upper troposphere.

### 562 **5.3 Water vapor anomaly**

563 To further assess the impact of TS Corentin and TC Enawo on the UTLS water vapor content, we compare the convolved  
564 CFH profiles to a monthly climatological MLS water vapor profile as there are no long-term stratospheric water vapor  
565 measurements at Réunion Island. For each year between 2004 and 2017, MLS water vapor profiles within  $\pm 5^\circ$  latitude and  
566  $\pm 10^\circ$  longitude of Réunion Island and over a period of 15 days surrounding the launch date, i.e. 10 January-9 February for 25  
567 January 2016 and 16 February-18 March 18 for 3 March 2017, are used to define a monthly climatological water vapor  
568 profile. We also computed a non-convective monthly climatological MLS water vapor profile by excluding MLS water  
569 vapor profiles with coincident low upper-tropospheric ozone (probably affected by convection, Paulik and Birner [2012]).  
570 The non-convective and monthly climatological MLS water vapor profile (using all profiles) look very similar (not shown).  
571 Thus, the climatological MLS water profile using all profiles is used for comparison with the water vapor measurements on  
572 25 January 2016 and 3 March 2017.

573 The monthly climatological MLS water vapor profiles and CFH convolved profiles are shown on Figure 9. Both monthly  
574 climatological water vapor profiles have comparable minimum water vapor mixing ratio at 83 hPa ( $3.5 \pm 0.6$  ppmv and  $3.3 \pm$   
575  $0.5$  ppmv for the January and March climatologies respectively). In the upper troposphere (316-178 hPa) the climatologies  
576 have mean values of  $277.6 \pm 269.2$  ppmv and  $266.1 \pm 253.2$  ppmv for January and March respectively. High variability in  
577 the UT is consistent with deep convection being more active during austral summer. Higher UT water vapor content in  
578 January relative to March is in agreement with the fact that the austral summer season reaches its peak in January/February.  
579 Both January and March climatologies have comparable TTL (147-68 hPa) water vapor content ( $5.3 \pm 1.8$  ppmv and  $5.1 \pm$   
580  $1.7$  ppmv for January and March respectively). The climatological mean stratospheric (56-22 hPa) value is  $4.2 \pm 1.3$  ppmv  
581 for both months.

582 Relative water vapor differences are defined with respect to the monthly climatological profile (i.e., relative difference =  
583  $(\text{CFH} - \text{MLS Climatology})/\text{MLS Climatology} \times 100$ ) and are displayed on the bottom panels of Figure 9. In addition to the

584 CFH convolved profile, we also compared the mean of MLS coincident profiles to the MLS monthly climatological profile  
585 for 25 January 2016 and 3 March 2017.

586 On 25 January 2016, the mean of MLS coincident profiles and the CFH convolved profile show a peak of  $\sim 30\%$  or  $7.7\text{ppmv}$   
587 in the relative difference with the MLS climatology in layer L1, but the pressure level of this peak differs in the two profiles  
588 with a peak at 178 hPa for the CFH convolved profile and 147 hPa for the mean of coincident MLS profiles.

589 To further evaluate the portion of the profiles that were influenced by convection, we calculated a convective fraction  
590 profile. For each pressure level depicted on Figure 9, 50,000 FLEXPART backtrajectories were initialized. A backtrajectory  
591 was tagged as convectively influenced when the IR BT observed by METEOSAT 7 falls below 230 K over the previous 7  
592 days, and if the altitude of the backtrajectory falls below 5 km, indicating a lower tropospheric origin. Hence, the convective  
593 fraction profile represents the percentage of trajectories for each pressure level that were considered as convective following  
594 those criterias. The convective fraction profile reaches a maximum of 60% at 147hPa, and confirms that layer L1 and the  
595 bottom part of layer L2 are convective. The FLEXPART backtrajectories from figure 6 and the values of the convective  
596 fraction profile confirm that the positive water vapor anomalies observed in layer L1 are associated with the convective  
597 outflow of TS Corentin.

598 On 3 March 2017, the hydration of the upper troposphere in layer L4 (between 215 and 121 hPa) is much more pronounced  
599 in the CFH convolved profile with a peak of value of  $\sim 180\%$  or  $45\text{ppmv}$  at 178 hPa. For the mean of MLS coincident  
600 profiles, the moistening is not as large with a relative difference of 36% or  $8.7\text{ppmv}$  at 178 hPa. The convective fraction  
601 profile had values of 60% at 178 and 147hPa, confirming that layer L4 were influenced by convection.

602 Ray and Rosenlof (2007) used measurements from AIRS to assess the impact of tropical cyclones in the Atlantic and Pacific  
603 basins on the amount of water vapor in the tropical UT. They showed that tropical cyclones can hydrate a deep layer of the  
604 surrounding upper troposphere by  $\sim 30\text{-}50$  ppmv or more within 500 km of the eye compared to the surrounding average  
605 water vapor mixing ratios (cf. Figure 3 of Ray and Rosenlof, 2007). They also looked at the evolution of UT water vapor  
606 changes as a function of the storm intensity as measured by the peak wind speed (cf. Figure 5 of Ray and Rosenlof, 2007). In  
607 both the Atlantic and western Pacific basins, the average water vapor at 223 hPa around the storm center steadily increased  
608 from 4 to 5 days prior to peak cyclone intensity to 2 days following peak cyclone intensity. The average water vapor  
609 enhancement in the two ocean basins was from 5 to 20 ppmv with an increase as high as 30-40 ppmv for some cyclones in  
610 the western Pacific. The CFH launch on 3 March 2017 18 UTC occurred 3.5 days before Enawo reached its peak intensity  
611 on 7 March at 06 UTC (pressure at the center of 932 hPa, ten-minute maximum sustained winds of  $204 \text{ km hr}^{-1}$ ) and the  
612 storm center was  $\sim 700$  km away from the island. Thus, deep convection associated with TC Enawo may have caused the

613 strong increase in UT water vapor observed on 3 March 2017. Ongoing work with MLS data to apply the methodology of  
614 Ray and Rosenlof (2007) to assess hydration of the UTLS by tropical cyclones for the 2004-2017 cyclone seasons in the  
615 southwest Indian Ocean is under way. This will be the focus of a future study but preliminary results indicate water vapor  
616 differences of 35% to 48% at between 178 and 261 hPa for categories 2 to 4 hurricanes on the Saffir-Simpson scale. Ray and  
617 Rosenlof (2007) indicated that tropical cyclones hydrate a deep layer of the UT in the vicinity of the cyclones by up to 50%  
618 above monthly mean water vapor mixing ratios. Therefore, our estimate of UT water vapor increases of 20 to 100% using  
619 CFH&MLS data for TS Coentim (Category 1 hurricane at its peak intensity) and TC Enawo (Category 4 hurricane at its  
620 peak intensity) are in broad agreement with our estimates based on the 2004-2017 MLS data and the study of Ray and  
621 Rosenlof (2007).

622 At 100 hPa (within layer L2), both MLS and CFH data are 20% (-0.7ppmv) below the climatological monthly mean values  
623 on 25 January 2016. This would be coherent with the near tropopause cooling observed on Figure 5 and the presence of deep  
624 convection around Réunion Island. In addition, TTL cirrus clouds were observed north of the island on both dates (Figure 5).  
625 Convectively generated or in-situ cirrus clouds in the TTL can dehydrate the tropopause region. Jensen et al. (1996) showed  
626 that ice clouds formed by large-scale vertical motions can result in depletion of water vapor mixing ratio by about 0.4 ppmv.  
627 Chae et al. (2011) investigated temperature and water vapor changes due to clouds in the TTL using MLS, CALIPSO and  
628 CloudSat datasets. They noted that generally clouds humidify the environment near 16 km (~100 hPa) or lower but  
629 dehydrate the TTL above 16 km.

630 On 25 January 2016, CFH and MLS data are 11% (+0.4 ppmv) and 18% (+0.7 ppmv) moister than the climatological values  
631 at 68 hPa (within layer L3), above the tropopause. Observational and modeling studies have indicated that overshooting  
632 convection can moisten the lower stratosphere by injecting water vapor or ice crystals directly above the overshooting clouds  
633 (e.g. Danielsen, 1993; Corti et al., 2008; Dauhut et al., 2015; Frey et al., 2015; Allison et al., 2018). In our case, the  
634 observation on 25 January 2016 was not made close to the deepest convective clouds that were ~1000 km north of the island  
635 (Figure 2), but was downwind of TS Coentim, as shown by the FLEXPART analysis (Figure 6). However, FLEXPART  
636 backtrajectories indicate that the air masses at 68h Pa (layer L3) originate from the South East Indian Ocean in the 20°S-  
637 30°S latitude band where the MLS water vapor anomaly for January 2016 is around 0.5 ppmv most likely due to the impact  
638 of the 2016 strong El Niño event. Hence, the positive anomaly against the climatological value can also be explained by  
639 horizontal advection from the South East Indian Ocean toward Reunion island.

640 It is difficult to conclude whether TC Enawo had a direct impact on water vapor in the lower stratosphere by using only the  
641 CFH observation on 3 March 2017. The FLEXPART analysis indicated that the CFH sounding did not sample the lower  
642 stratosphere downwind of Enawo.

643 Ongoing work with the mesoscale model Meso-NH at a 2-km resolution for TC Enawo for the period 2-7 March 2017  
644 indicates that deep convective clouds within 500 km of the cyclone eye can inject ice crystals and moisten the lower  
645 stratosphere, resulting in an average anomaly of  $\sim 2$ ppmv within 500 km of the tropical cyclone eye. The strongest  
646 humidification in the lower stratosphere (17-19 km;  $\sim 88$ -66 hPa) was found after March 4 when the storm stalled over the  
647 ocean (while intensifying) and after March 6 when it reached its peak intensity. Thus, the CFH observation on 3 March 2017  
648 was made before TC Enawo had influenced the lower stratosphere above 100 hPa. This is further confirmed by the fact  
649 CALIOP did not have a lower stratospheric signal on Figure 6.

650 Tropical cyclones are unique among tropical convective systems in that they persist for many days and thus could affect the  
651 UTLS more than other mesoscale convective systems. Clouds in tropical cyclones often reach to and sometimes beyond the  
652 tropopause (e.g., Romps and Kuang 2009). Allison et al. (2018) have investigated the vertical transport of water vapor by the  
653 2013 tropical cyclone Ingrid in the North Atlantic. Results of their high-resolution numerical simulations indicated that  
654 hydration occurred between 17.5 and 21 km (83 to 56 hPa) due to the injection of ice crystals. As the exact role of deep  
655 convection, and tropical cyclones in particular, in hydrating the lower stratosphere is still under debate, additional TTL  
656 observations of water vapor and modeling work are needed to quantify the overall impact of convection on TTL and LS  
657 water vapor. High-resolution (2 km) numerical simulations of TC Enawo for the period 2-7 March 2017 are underway to  
658 gain a closer look at the effect of TC convection on TTL temperature and water vapor. This work will be the subject of a  
659 subsequent study.

## 660 **7 Summary**

661 Two balloon launches from the Mado Observatory were specifically planned using the FLEXPART Lagrangian model and  
662 METEOSAT 7 infrared images to sample the convective outflow from Tropical Storm Corentin on 25 January 2016 and  
663 Tropical Cyclone Enawo on 3 March 2017. Balloon-borne measurements of CFH water vapor, ozone and iMET temperature  
664 and water vapor lidar measurements, showed that both storms humidified the TTL, with  $RH_{ice}$  values exceeding 50% for TS  
665 Corentin and 90% for TC Enawo in the upper troposphere. Comparing the two CFH profiles to the climatological monthly  
666 mean MLS water vapor profiles, positive anomalies of water vapor were identified with peak values of 7.7 ppmv for TS  
667 Corentin and 45 ppmv for TC Enawo at 17hPa. According to the FLEXPART backtrajectories and METEOSAT 7 infrared  
668 images, those air masses originated from convectively active regions of TS Corentin and TC Enawo and were lifted from the  
669 lower troposphere to the upper troposphere around one day before the planned balloon launches. In addition, the CALIOP  
670 satellite measurements indicated cirrus clouds north of Réunion Island for the same altitude range for both storms.

671 According to the CFH profile on 25 January 2016 and MLS climatology, air masses measured near the tropopause were

672 anomalously dry around 100 hPa and anomalously wet around 68 hPa in the lower stratosphere. FLEXPART  
673 backtrajectories were used to find the origin of these layers that could be traced back to TS Coentim upper-tropospheric  
674 divergent flow and active convective regions. Deep convective clouds and cirrus clouds may have dehydrated the region  
675 around 100hPa. According to FLEXPART backtrajectories, the positive anomaly at 68hPa can be explained by a horizontal  
676 transport from the South East Indian Ocean. The South East Indian Ocean had a positive water vapor anomaly of  $\sim 0.5$ ppmv  
677 in January 2016 most likely due to the strong 2016 El Niño event (Avery et al., 2017).

678 On the contrary, no water vapor anomaly was found near or above the tropopause on 3 March 2017 as the tropopause region  
679 was not downwind of TC Enawo. According to FLEXPART backtrajectories, those air masses stayed away from the upper-  
680 tropospheric dynamics of TC Enawo and its convective active regions. Hence the tropopause region on 3 March 2017 was  
681 not affected by Enawo, at least not at the time of the balloon launch and at this stage of Enawo's development.

682 This study showed the impact of two tropical cyclones on the humidification of the TTL. It also demonstrates the need to  
683 develop balloon borne high precision observations in regions where TTL in-situ observations are sparse, such as the tropics  
684 and the SWIO in particular. High-resolution accurate observations of water vapor are needed to document the impact of  
685 tropical cyclones and deep convection in general on the TTL. The impact of tropical cyclones on the TTL water vapor  
686 budget will be analyzed in a more quantitative way using MLS data and tropical cyclones best tracks from 2004 to 2017 in a  
687 subsequent paper. In addition, the impact of deep convection and overshooting clouds within TC Enawo on the water vapor  
688 budget of the TTL will be analyzed using high-resolution (2 km) mesoscale simulation of TC Enawo.

689 *Data availability.* MLS water vapor data used in this study are available at <https://mls.jpl.nasa.gov/> and CALIPSO L1B lidar  
690 data are available at [https://eosweb.larc.nasa.gov/project/calipso/lidar\\_l1b\\_profile\\_table](https://eosweb.larc.nasa.gov/project/calipso/lidar_l1b_profile_table). The NDACC/SHADOZ ozone  
691 measurements for Réunion Island are available at <https://tropo.gsfc.nasa.gov/shadoz/Reunion.html>. The SWOOSH dataset is  
692 available at <https://data.nodc.noaa.gov/cgi-bin/iso?id=gov.noaa.ncdc:C00958>. The CFH and lidar water vapor data are  
693 available from the authors (SE, VD, PK) upon request. The FLEXPART Lagrangian trajectories can be requested from the  
694 corresponding author Stephanie Evan ([stephanie.evan@univ-reunion.fr](mailto:stephanie.evan@univ-reunion.fr)).

695

696 *Author contributions.* All authors contributed to the paper. SE wrote the manuscript with contributions from JB, KR, SD,  
697 DH, FP, JMM, VD, GP, HV, PK, JPC. SE, JB, FP, JMM, DH, JPC, VD, GP and HV performed the CFH/Ozone/Lidar  
698 measurements. HV processed the CFH data. SE and JB performed the FLEXPART simulations. SM provided the SWOOSH  
699 dataset. All authors revised the manuscript draft.



700 *Competing interests.* The authors declare that they have no conflict of interest.

701 *Acknowledgments*

702 We thank the Aura Science Team for the MLS data (<https://mls.jpl.nasa.gov/>) and the CALIPSO science team for the L1B  
703 lidar data ([https://eosweb.larc.nasa.gov/project/calipso/lidar\\_l1b\\_profile\\_table](https://eosweb.larc.nasa.gov/project/calipso/lidar_l1b_profile_table)).

704 OPAR (Observatoire de Physique de l'Atmosphère à La Réunion, including Maïdo Observatory) is part of OSU-R  
705 (Observatoire des Sciences de l'Univers à La Réunion) which is being funded by Université de la Réunion, CNRS-INSU,  
706 Météo-France, and the french research infrastructure ACTRIS-France (Aerosols, Clouds and Trace gases Research  
707 Infrastructure). OPAR's water vapor lidar and ozone radiosounding belong to the international network NDACC (Network  
708 for the Detection of Atmospheric Composition Change). This work was supported by the French LEFE CNRS-INSU  
709 Program (VAPEURDO).

710 S. Evan thanks Susanne Koerner (DWD/GRUAN Leadcentre, Germany) for her training on the CFH instrument.

711 **References**

712 Allison, T., Fuelberg, H., and Heath, N.: Simulations of vertical water vapor transport for TC Ingrid (2013), *J. Geophys.*  
713 *Res.*, 123, 8255-8282, <https://doi.org/10.1029/2018JD028334>, 2018.

714 Avery, M. A., Davis, S. M., Rosenlof, K. H., Ye, H., and Dessler, A.: Large anomalies in lower stratospheric water vapor  
715 and ice during the 2015-2016 El Niño, *Nat. Geosci.*, 10, 405-409. <https://doi.org/10.1038/ngeo2961>, 2017.

716 Baldwin, M. P., Gray, L. J., Dunkerton, T. J., Hamilton, K., Haynes, P. H., Holton, J. R., Alexander, M. J., Hirota, I.,  
717 Horinouchi, T., Jones, D. B. A., Marquardt, C., Sato, K., and Takahashi, M.: The quasi-biennial oscillation, *Rev. Geophys.*,  
718 <https://doi.org/10.1029/1999RG000073>, 2001

719 Baray J.-L., Y. Courcoux, P. Keckhut, T. Portafaix, P. Tulet, J.-P. Cammas, A. Hauchecorne, S. Godin-Beekmann, M. De  
720 Mazière, C. Hermans, F. Desmet, K. Sellegri, A. Colomb, M. Ramonet, J. Sciare, C. Vuillemin, C. Hoareau, D. Dionisi, V.  
721 Duflot, H. Vérémes, J. Porteneuve, F. Gabarrot, T. Gaudo, J.-M. Metzger, G. Payen, J. Leclair de Bellevue, C. Barthe, F.  
722 Posny, P. Ricaud, A. Abchiche, and R. Delmas, Maïdo observatory: a new high-altitude station facility at Reunion Island  
723 (21° S, 55°E) for long-term atmospheric remote sensing and in situ measurements, *Atmos. Meas. Tech.*, 6, 2865-2877, 2013

724 Bechtold, P., Köhler, M., Jung, T., Doblas-Reyes, F., Leutbecher, M., Rodwell, M. J., Vitart, F. and Balsamo, G., *Advances*

725 in simulating atmospheric variability with the ECMWF model: From synoptic to decadal time-scales., *Q. J. Roy. Meteorol.*  
726 *Soc* 134: 1337-1351, <https://doi:10.1002/qj.289>, 2008.

727 Bechtold, P., Semane, N., Lopez, P., Chaboureaud, J.-P., Beljaars, A., and Bormann, N., Representing Equilibrium and  
728 Nonequilibrium Convection in Large-Scale Models, *J. Atmos. Sci.*, 71, 734–753, <https://doi.org/10.1175/JAS-D-13-0163.1>,  
729 2014.

730 Bodeker, G. E., Bojinski, S., Cimini, D., Dirksen, R. J., Haefelin, M., Hannigan, J. W., Hurst, D., Madonna, F., Maturilli,  
731 M., Mikalsen, A. C., Philipona, R., Reale, T., Seidel, D. J., Tan, D. G. H., Thorne, P. W., Vömel, H., and Wang, J.:  
732 Reference upper-air observations for climate: From concept to reality, *B. Am. Meteorol. Soc.*, 97, 123–135,  
733 <https://doi.org/10.1175/BAMS-D-14-00072.1>, 2015.

734 Bovalo, C., C. Barthe, and N. Bègue, A lightning climatology of the South West Indian Ocean, *Nat. Hazards Earth Syst. Sci.*,  
735 12, 2659–2670, <https://doi:10.5194/nhess-12-2659-2012>, 2012.

736 Brunamonti, S., Jorge, T., Oelsner, P., Hanumanthu, S., Singh, B. B., Kumar, K. R., Sonbawne, S., Meier, S., Singh, D.,  
737 Wienhold, F. G., Luo, B. P., Boettcher, M., Poltera, Y., Jauhiainen, H., Kayastha, R., Karmacharya, J., Dirksen, R., Naja, M.,  
738 Rex, M., Fadnavis, S., and Peter, T.: Balloon-borne measurements of temperature, water vapor, ozone and aerosol  
739 backscatter on the southern slopes of the Himalayas during StratoClim 2016–2017, *Atmos. Chem. Phys.*, 18, 15937–15957,  
740 <https://doi.org/10.5194/acp-18-15937-2018>, 2018.

741 Cairo, F., Buontempo, C., MacKenzie, A. R., Schiller, C., Volk, C. M., Adriani, A., Mitev, V., Matthey, R., Di  
742 Donfrancesco, G., Oulanovsky, A., Ravegnani, F., Yushkov, V., Snels, M., Cagnazzo, C., and Stefanutti, L.: Morphology of  
743 the tropopause layer and lower stratosphere above a tropical cyclone: a case study on cyclone Davina (1999), *Atmos. Chem.*  
744 *Phys.*, 8, 3411–3426, <https://doi.org/10.5194/acp-8-3411-5-2008>, 2008.

745 Chae, J. H., Wu, D. L., Read, W. G., and Sherwood, S. C.: The role of tropical deep convective clouds on temperature, water  
746 vapor, and dehydration in the tropical tropopause layer (TTL), *Atmos. Chem. Phys.*, 11, 3811–3821,  
747 <https://doi.org/10.5194/acp-11-3811-2011>, 2011.

748 Chiang, J.C. and A.H. Sobel, Tropical Tropospheric Temperature Variations Caused by ENSO and Their Influence on the  
749 Remote Tropical Climate. *J. Climate*, 15, 2616-2631, [https://doi.org/10.1175/1520-0442\(2002\)015<2616:TTTTVCB>2.0.CO;2](https://doi.org/10.1175/1520-0442(2002)015<2616:TTTTVCB>2.0.CO;2), 2012

751 Corti, T., Luo, B. P., de Reus, M., Brunner, D., Cairo, F., Mahoney, M. J., Martucci, G., Matthey, R., Mitev, V., dos Santos,  
752 F. H., Schiller, C., Shur, G., Sitnikov, N. M., Spelten, N., Vössing, H. J., Borrmann, S., and Peter, T.: Unprecedented  
753 evidence for deep convection hydrating the tropical stratosphere, *Geophys. Res. Lett.*, 35, L10810,  
754 <https://doi.org/10.1029/2008GL033641>, 2008.

755 Danielsen, E. F.: A dehydration mechanism for the stratosphere, *Geophys. Res. Lett.*, 9, 605–608, 1982.

756 Dauhut, T., Chaboureaud, J. P., Escobar, J., and Mascart, P.: Large-eddy simulations of the convective making the  
757 stratosphere wetter, *Atmos. Sci. Lett.*, 16, 135–140, <https://doi.org/10.1002/asl2.534>, 2015.

758 Davis, S. M., Rosenlof, K. H., Hassler, B., Hurst, D. F., Read, W. G., Vömel, H., Selkirk, H., Fujiwara, M., and Damadeo,  
759 R.: The Stratospheric Water and Ozone Satellite Homogenized (SWOOSH) database: a long-term database for climate  
760 studies, *Earth Syst. Sci. Data*, 8, 461–490, <https://doi.org/10.5194/essd-8-461-2016>, 2016.

761 Davis, S. M., Liang, C. K., and Rosenlof, K. H.: Interannual variability of tropical tropopause layer clouds, *Geophys. Res.*  
762 *Lett.*, 40, 2862–2866. <https://doi.org/10.1002/grl.50512>, 2013.

763 Dessler, A. E. and Sherwood, S. C.: A model of HDO in the tropical tropopause layer, *Atmos. Chem. Phys.*, 3, 2173–2181,  
764 <https://doi.org/10.5194/acp-3-2173-2003>, 2003.

765 Emanuel, K. A., and Zivkovic, M.: Development and evaluation of a convection scheme for use in climate  
766 models, *J. Atmos. Sci.*, 56, 1766–1782, 1999.

767 Folkins, I. and R.V. Martin: The Vertical Structure of Tropical Convection and Its Impact on the Budgets of Water Vapor  
768 and Ozone. *J. Atmos. Sci.*, 62, 1560–1573, <https://doi.org/10.1175/JAS3407.1>, 2005.

769 Frey, W., Schofield, R., Hoor, P., Kunkel, D., Ravegnani, F., Ulanovsky, A., Viciani, S., D'Amato, F., and Lane, T. P.: The  
770 impact of overshooting deep convection on local transport and mixing in the tropical upper troposphere/lower stratosphere  
771 (UTLS), *Atmos. Chem. Phys.*, 15, 6467–6486, <https://doi.org/10.5194/acp-15-6467-2015>, 2015.

772 Fueglistaler, S., Dessler, A. E., Dunkerton, T. J., Folkins, I., Fu, Q., and Mote, P. W.: Tropical tropopause layer, *Rev.*  
773 *Geophys.*, 47, RG1004, <https://doi.org/10.1029/2008RG000267>, 2009.

774 Goff, J. A. and Gratch, S., Low-pressure properties of water from –160 to 212 F. *Trans. Am. Soc. Heating Air-Cond. Eng.*,  
775 52, 95–122 (presented at the 52nd annual meeting of the American society of heating and ventilating engineers, New York),

776 1946.

777 Hartmann, D.L, Holton J.R. and Q. Fu, The heat balance of the tropical tropopause, cirrus, and stratospheric dehydration.  
778 *Geophys. Res. Lett.*, 28, <https://doi.org/10.1029/2000GL012833>, 2001.

779 Highwood, E. J. and Hoskins, B. J.: The tropical tropopause, *Q. J. Roy. Meteorol. Soc.*, 124, 1579-1604,  
780 <https://doi.org/10.1002/qj.49712454911>, 1998.

781 Ho C-H, Kim J-H, Jeong J-H, Kim H-S, and Chen D.: Variation of tropical cyclone activity in the South Indian Ocean: El  
782 Niño-Southern Oscillation and Madden-Julian Oscillation effects. *J. Geophys. Res.*, 111: D22101,  
783 <https://doi.org/10.1029/2006JD007289>, 2006

784 Holloway, C.E, and J.D. Neelin: The convective cold top and quasi equilibrium. *J. Atmos. Sci.* 64,  
785 1467–1487.[doi:10.1175/JAS3907.1](https://doi.org/10.1175/JAS3907.1), 2007.

786 Holton, J. R., and A. Gettelman: Horizontal transport and the dehydration of the stratosphere. *Geophys. Res. Lett.*, 28, 2799–  
787 2802, <https://doi.org/10.1029/2001GL013148>, 2001.

788  
789 Hurst, D. F., Hall, E. G., Jordan, A. F., Miloshevich, L. M., Whiteman, D. N., Leblanc, T., Walsh, D., Vömel, H., and  
790 Oltmans, S. J.: Comparisons of temperature, pressure and humidity measurements by balloon-borne radiosondes and frost  
791 point hygrometers during MOHAVE-2009, *Atmos. Meas. Tech.*, 4, 2777–2793, <https://doi.org/10.5194/amt-4-2777-2011>,  
792 2011.

793 Hurst, D. F., Lambert, A., Read, W. G., Davis, S. M., Rosenlof, K. H., Hall, E. G., Jordan, A. F., and Oltmans, S. J.:  
794 Validation of Aura Microwave Limb Sounder stratospheric water vapor measurements by the NOAA frost point hygrometer,  
795 *J. Geophys. Res.-Atmos.*, 119, 1612–1625, [doi:10.1002/2013jd020757](https://doi.org/10.1002/2013jd020757), 2014

796 Jensen, E. J., O. B. Toon, H. B. Selkirk, J. D. Spinhirne, and Schoeberl M. R.: On the formation and persistence of subvisible  
797 cirrus clouds near the tropical tropopause, *J. Geophys. Res.*, 101, 21,361–21,375, 1996.

798 Jensen, E. J., Ackerman, A. S., and Smith, J. A.: Can overshooting convection dehydrate the tropical tropopause layer?, *J.*  
799 *Geophys. Res.-Atmos.*, 112, D11209, [doi:10.1029/2006JD007943](https://doi.org/10.1029/2006JD007943), 2007.

800 Jensen, E. J., Pfister, L., Jordan, D. E., Bui, T. V., Ueyama, R., Singh, H. B., Thornberry, T. D., Rollins, A. W., Gao, R.,  
801 Fahey, D. W., Rosenlof, K. H., Elkins, J. W., Diskin, G. S., DiGangi, J. P., Lawson, R. P., Woods, S., Atlas, E. L., Navarro  
802 Rodriguez, M. A., Wofsy, S. C., Pittman, J., Bardeen, C. G., Toon, O. B., Kindel, B. C., Newman, P. A., McGill, M. J.,  
803 Hlavka, D. L., Lait, L. R., Schoeberl, M. R., Bergman, J. W., Selkirk, H. B., Alexander, M. J., Kim, J.-E., Lim, B. H., Stutz,

804 J., and Pfeilsticker, K.: The NASA Airborne Tropical Tropopause Experiment: High-Altitude Aircraft Measurements in the  
805 Tropical Western Pacific, *B. Am. Meteorol. Soc.*, 98, 129–143, <https://doi.org/10.1175/BAMS-D-14-00263.1>, 2017.

806 [Jorge, T., Brunamonti, S., Poltera, Y., Wienhold, F. G., Luo, B. P., Oelsner, P., Hanumanthu, S., Sing, B. B., Körner, S.,  
807 Dirksen, R., Naja, M., Fadnavis, S., and Peter, T.: Understanding cryogenic frost point hygrometer measurements after  
808 contamination by mixed-phase clouds, \*Atmos. Meas. Tech. Discuss.\*, <https://doi.org/10.5194/amt-2020-176>, in review, 2020](#)

809

810 Keckhut, P., Courcoux, Y., Baray, J.-L., Porteneuve, J., Vèrèmes, H., Hauchecorne, A., Dionisi, D., Posny, F., Cammas, J.-  
811 P., Payen, G., Gabarrot, F., Evan, S., Khaykin, S., Rüfenacht, R., Tschanz, B., Kämpfer, N., Ricaud, P., Abchiche, A.,  
812 Leclairde-Bellevue, J., and Dufлот, V.: Introduction to the Maïdo Lidar Calibration Campaign dedicated to the validation of  
813 upper air meteorological parameters, *J. Appl. Remote Sens.*, 9, 094099, <https://doi.org/10.1117/1.JRS.9.094099>, 2015.

814 Khaykin, S. M., Engel, I., Vömel, H., Formanyuk, I. M., Kivi, R., Korshunov, L. I., Krämer, M., Lykov, A. D., Meier, S.,  
815 Naebert, T., Pitts, M. C., Santee, M. L., Spelten, N., Wienhold, F. G., Yushkov, V. A., and Peter, T.: Arctic stratospheric  
816 dehydration – Part 1: Unprecedented observation of vertical redistribution of water, *Atmos. Chem. Phys.*, 13, 11503–11517,  
817 <https://doi.org/10.5194/acp-13-11503-2013>, 2013.

818 Kuang, Z., and C. S. Bretherton: Convective influence on the heat balance of the tropical tropopause layer: A cloud-  
819 resolving model study, *J. Atmos. Sci.*, 61, 2919–2927, <https://doi.org/10.1175/JAS-3306.1>, 2004.

820 Lee, S.-K., Park, W., Baringer, M. O., Gordon, A. L., Huber, B., and Liu, Y.: Pacific origin of the abrupt increase in Indian  
821 Ocean heat content during the warming hiatus, *Nat. Geosci.*, 8(6), 445–449, 2015.

822 Liu, C. and Zipser, E. J.: Global distribution of convection penetrating the tropical tropopause, *J. Geophys. Res.*, 110,  
823 D23104, <https://doi.org/10.1029/2005JD006063>, 2005.

824 Magnusson, L., J.-R. Bidlot, M. Bonavita, A. R. Brown, P. A. Browne, G. De Chiara, M. Dahoui, S. T. K. Lang, T. McNally,  
825 K. S. Mogensen, F. Pappenberger, F. Prates, F. Rabier, D. S. Richardson, F. Vitart, and S. Malardel: ECMWF Activities for  
826 improved hurricane forecasts, <https://doi.org/10.1175/BAMS-D-18-0044.1>, 2018

827 Neumann, C.J.: "Global Overview" - Chapter 1" [Global Guide to Tropical Cyclone Forecasting](#), WMO/TC-No. 560, Report  
828 No. TCP-31, World Meteorological Organization; Geneva, Switzerland, 1993

829 Paulik, L. C. and Birner, T.: Quantifying the deep convective temperature signal within the tropical tropopause layer (TTL),  
830 Atmos. Chem. Phys., 12, 12183-12195, <https://doi.org/10.5194/acp-12-12183-2012>, 2012.

831 Randel, W. J., F. Wu, and W. Rivera Rios: Thermal variability of the tropical tropopause region derived from GPS/MET  
832 observations, J. Geophys. Res., 108(D1), 4024, <https://doi:10.1029/2002JD002595>, 2003

833 Ray, E. A., and Rosenlof, K. H.; Hydration of the upper troposphere by tropical cyclones, J. Geophys. Res., 112, D12311,  
834 <https://doi:10.1029/2006JD008009>, 2007.

835 Read, W. G., Lambert, A., Bacmeister, J., Cofield, R. E., Christensen, L. E., Cuddy, D. T., Daffer, W. H., Drouin, B. J.,  
836 Fetzer, E., Froidevaux, L., Fuller, R., Herman, R., Jarnot, R. F., Jiang, J. H., Jiang, Y. B., Kelly, K., Knosp, B. W.,  
837 Kovalenko, L. J., Livesey, N. J., Liu, H. C., Manney, G. L., Pickett, H. M., Pumphrey, H. C., Rosenlof, K. H., Sabounchi,  
838 X., Santee, M. L., Schwartz, M. J., Snyder, W. V., Stek, P. C., Su, H., Takacs, L. L., Thurstans, R. P., Vomel, H., Wagner, P.  
839 A., Waters, J. W., Webster, C. R., Weinstock, E. M., and Wu, D. L.: Aura Microwave Limb Sounder upper tropospheric and  
840 lower stratospheric H<sub>2</sub>O and relative humidity with respect to ice validation, J. Geophys. Res.-Atmos., 112, D24S35  
841 [doi:10.1029/2007JD008752](https://doi:10.1029/2007JD008752), 2007.

842 Roca, R., M. Viollier, L. Picon, and Desbois M.: A multisatellite analysis of deep convection and its moist environment  
843 over the Indian Ocean during the winter monsoon, J. Geophys. Res., 107(D19), 8012, [doi:10.1029/2000JD000040](https://doi:10.1029/2000JD000040), 2002.

844 Romps, D. M., and Kuang, Z.: Overshooting convection in tropical cyclones, Geophys. Res. Lett., 36, L09804,  
845 <https://doi:10.1029/2009GL037396>, 2009

846 Schoeberl, M. R., Dessler, A. E., Wang, T., Avery, M. A., and Jensen, E. J.: Cloud formation, convection, and stratospheric  
847 dehydration, Earth and Space Science, 1, 1-17, [doi:10.1002/2014EA000014](https://doi:10.1002/2014EA000014), 2014

848 Sherwood, S.C., Horinouchi, T., and Zeleznik, H.A.: Convective Impact on Temperatures Observed near the Tropical  
849 Tropopause. J. Atmos. Sci., 60, 1847–1856, [https://doi.org/10.1175/1520-0469\(2003\)060<1847:CIOTON>2.0.CO;2](https://doi.org/10.1175/1520-0469(2003)060<1847:CIOTON>2.0.CO;2), 2003

850 Stohl, A., Forster, C., Frank, A., Seibert, P., and Wotawa, G.: Technical note: The Lagrangian particle dispersion model  
851 FLEXPART version 6.2, Atmos. Chem. Phys., 5, 2461-2474, <https://doi.org/10.5194/acp-5-2461-2005>, 2005.

852 Soden, B.J.: The Sensitivity of the Tropical Hydrological Cycle to ENSO. J. Climate, 13, 538–549,  
853 [https://doi.org/10.1175/1520-0442\(2000\)013<0538:TSOTTH>2.0.CO;2](https://doi.org/10.1175/1520-0442(2000)013<0538:TSOTTH>2.0.CO;2), 2000

854 Tao, C. and H. Jiang: Global Distribution of Hot Towers in Tropical Cyclones Based on 11-Yr TRMM Data. *J. Climate*, 26,  
855 1371–1386, <https://doi.org/10.1175/JCLI-D-12-00291.1>, 2013.

856 Tian, E. W., Su, H., Tian, B., and Jiang, J. H. (2019). Interannual variations of water vapor in the tropical upper troposphere  
857 and the lower and middle stratosphere and their connections to ENSO and QBO, *Atmospheric Chemistry and Physics*, 19,  
858 9913-9926, doi:10.5194/acp-19-9913-2019.

859 Tiedtke, M.: A Comprehensive Mass Flux Scheme for Cumulus Parameterization in Large-Scale Models, *Mon. Weather*  
860 *Rev.*, 117, 1779–1800, [https://doi.org/10.1175/1520-0493\(1989\)117<1779:ACMFSF>2.0.CO;2](https://doi.org/10.1175/1520-0493(1989)117<1779:ACMFSF>2.0.CO;2), 1989

861 Tissier, A.-S. and Legras, B.: Convective sources of trajectories traversing the tropical tropopause layer, *Atmos. Chem.*  
862 *Phys.*, 16, 3383–3398, <https://doi.org/10.5194/acp-16-3383-2016>, 2016.

863 Thompson, A. M., Witte, J. C., McPeters, R. D., Oltmans, S. J., Schmidlin, F. J., Logan, J. A., Fujiwara, M., Kirchhoff, V.  
864 W. J. H., Posny, F., Coetzee, G. J. R., Hoegger, B., Kawakami, S., Ogawa, T., Johnson, B. J., Vömel, H., and Labow, G.:  
865 Southern Hemisphere Additional Ozonesondes (SHADOZ) 1998–2000 tropical ozone climatology 1. Comparison with Total  
866 Ozone Mapping Spectrometer (TOMS) and ground-based measurements, *J. Geophys. Res.-Atmos.*, 108, 8238,  
867 doi:10.1029/2001jd000967, 2003.

868 Toon, O. B., Starr, D. O., Jensen, E. J., Newman, P. A., Platnick, S., Schoeberl, M. R., Wennberg, P. O., Wofsy, S. C.,  
869 Kurylo, M. J., Maring, H., Jucks, K. W., Craig, M. S., Vasques, M. F., Pfister, L., Rosenlof, K. H., Selkirk, H. B., Colarco,  
870 P. R., Kawa, S. R., Mace, G. G., Minnis, P., and Pickering, K. E.: Planning, implementation, and first results of the Tropical  
871 Composition, Cloud and Climate Coupling Experiment (TC4), *J. Geophys. Res.*, 115, D00J04,  
872 <https://doi.org/10.1029/2009JD013073>, 2010.

873 Ueyama, R., Jensen, E. J., Pfister, L., and Kim, J.-E.: Dynamical, convective, and microphysical control on wintertime  
874 distributions of water vapor and clouds in the tropical tropopause layer, *J. Geophys. Res.-Atmos.*, 120, 10483-10500, <https://doi.org/10.1002/2015JD023318>, 2015.

876 Ueyama, R., Jensen, E. J., and Pfister, L.: Convective influence on the humidity and clouds in the tropical tropopause layer  
877 during boreal summer. *J. Geophys. Res. Atmos.*, 123, 7576-7593, <https://doi.org/10.1029/2018JD028674>, 2018.

878 Vaughan, M., S. Young, D. Winker, K. Powell, A. Omar, Z. Liu, Y. Hu, and C. Hostetler: Fully automated analysis of space-  
879 based lidar data: An overview of the CALIPSO retrieval algorithms and data products. *Proc. SPIE Int. Soc. Opt. Eng.*, 5575,

880 16-30, 2004.

881 Vèrèmes, H., Payen, G., Keckhut, P., Duflot, V., Baray, J.-L., Cammas, J.-P., Evan, S., Posny, F., Körner, S. and Bosser, P.:  
882 Validation of the Water Vapor Profiles of the Raman Lidar at the Maïdo Observatory (Reunion Island) Calibrated with  
883 Global Navigation Satellite System Integrated Water Vapor. *Atmosphere*, 10, 713, 2019

884 Vömel, H., Barnes, J. E., Forno, R. N., Fujiwara, M., Hasebe, F., Iwasaki, S., Kivi, R., Komala, N., Kyrö, E., Leblanc, T.,  
885 Morel, B., Ogino, S. Y., Read, W. G., Ryan, S. C., Saraspriya, S., Selkirk, H., Shiotani, M., Canossa, J. V., and Whiteman,  
886 D. N.: Validation of Aura Microwave Limb Sounder water vapor by balloonborne Cryogenic Frost point Hygrometer  
887 measurements, *J. Geophys. Res.-Atmos.*, 112, D24S37, doi:10.1029/2007JD008698, 2007a.

888 Vömel, H., Naebert, T., Dirksen, R., and Sommer, M.: An update on the uncertainties of water vapor measurements using  
889 cryogenic frost point hygrometers, *Atmos. Meas. Tech.*, 9, 3755–3768, <https://doi.org/10.5194/amt-9-3755-2016>, 2016.

890 Witte J. C., Thompson, A. M., Smit, H. G. J., Fujiwara, M., Posny, F., Coetzee, G. J. R., Northam, E. T., Johnson, B. J.,  
891 Sterling, C. W., Mohammed, M., Ogino, S.-Y., Jordan, A., daSilva, F. R., and Zainal, Z.: First reprocessing of Southern  
892 Hemisphere ADditional OZonesondes (SHADOZ) profile records (1998–2015) 1: Methodology and evaluation, *J. Geophys.*  
893 *Res.*, 122, 6611–6636, <https://doi.org/10.1002/2016JD026403>, 2017.

894 Yan, X., Wright, J. S., Zheng, X., Livesey, N. J., Vömel, H., and Zhou, X.: Validation of Aura MLS retrievals of  
895 temperature, water vapour and ozone in the upper troposphere and lower–middle stratosphere over the Tibetan Plateau  
896 during boreal summer, *Atmos. Meas. Tech.*, 9, 3547–3566, <https://doi.org/10.5194/amt-9-3547-2016>, 2016.

897 Yuan, W., Geller, M. A. and Love, P. T.: ENSO influence on QBO modulations of the tropical tropopause. *Q. J. Roy.*  
898 *Meteorol. Soc.*, 140: 1670-1676. <https://doi.org/10.1002/qj.2247>, 2014

899 Yulaeva, E. and Wallace, J. M.: The Signature of ENSO in Global Temperature and Precipitation Fields Derived from the  
900 Microwave Sounding Unit, *J. Climate*, 7, 1719-1736, [https://doi.org/10.1175/1520-0442\(1994\)0072.0.co;2](https://doi.org/10.1175/1520-0442(1994)0072.0.co;2), 1994

901 Yulaeva, E., Holton, J. R., and Wallace, J. M.: On the Cause of the Annual Cycle in Tropical Lower-Stratospheric  
902 Temperatures, *J. Atmos. Sci.*, 51(2), 169-174, 1994.

903 Zhou, X. L., Geller, M. A., and Zhang, M. H.: Tropical cold point tropopause characteristics derived from ECMWF  
904 reanalyses and soundings, *J. Climate*, 14, 1823–1838, [https://doi.org/10.1175/1520-0442\(2001\)0142.0.co;2](https://doi.org/10.1175/1520-0442(2001)0142.0.co;2), 2001.



905 Zhou, X. L., and J. R. Holton: Intraseasonal variations of tropical cold point tropopause temperatures. J. Climate, 15, 1460-  
906 1473, 2002

907

908

909

910

911

912

913

914

915

916

917

918

919

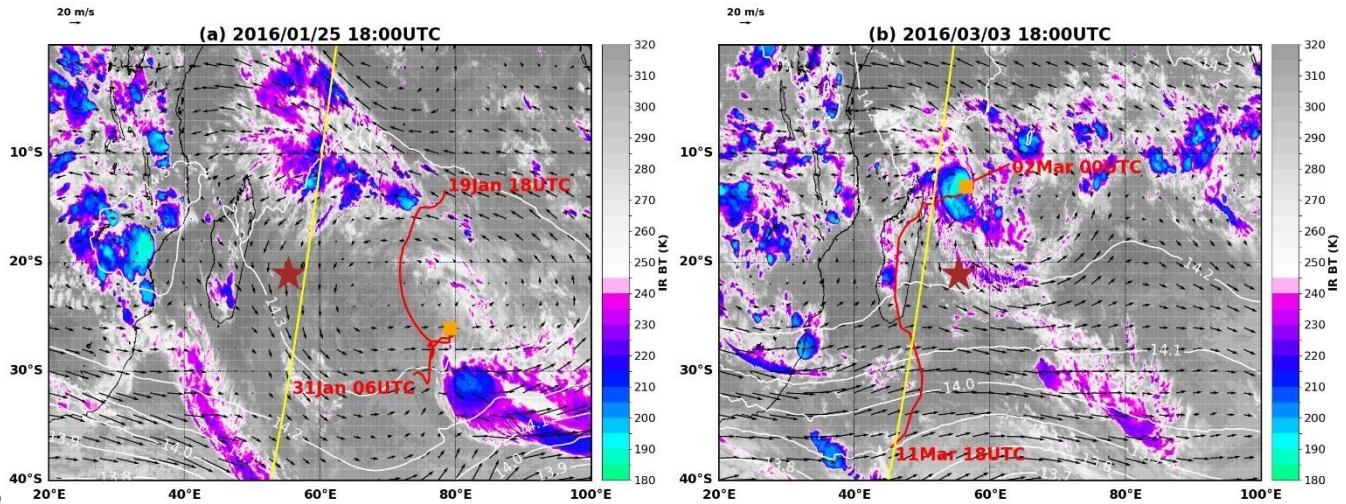
920 **Table 1:** CPT properties (temperature and height) from the radiosonde launches on 25 January 2016/3 March 2017 and NDACC/SHADOZ  
921 seasonal mean (December-March) CPT properties (for the period 1997-2017).

922

	Observations	CPT T (K)	CPT altitude (km)
mean SHADOZ Dec-March (1997-2017)	200	193.90 ( $\pm 2.26$ )	17.31 ( $\pm 0.71$ )
Profile on 25 January 2016	1	192.64	17.30
Profile on 3 March 2017	1	194.58	16.10

923

924



926

927

928 **Figure 1:** Infrared ( $10.8 \mu\text{m}$ ) brightness temperature (K) observed by METEOSAT-7 at the time of the CFH launch for a) 25  
 929 January 2016 at 18 UTC and b) 3 March 2017 at 18 UTC. The red lines correspond to the best tracks of tropical cyclones  
 930 Corentin (19-31 January 2016) and Enawo (02-11 March 2017). The orange squares indicate the positions of the TC centers  
 931 (defined as the minimum pressure in the Météo-France best track data) at the time of the satellite observation. The brown stars  
 932 indicate the position of the Maïdo Observatory on Réunion Island ( $21.08^\circ\text{S}$ ,  $55.38^\circ\text{E}$ ). The yellow lines correspond to  
 933 CALIPSO orbit tracks on 25 January 2016 at 21:06 UTC and 3 March 2017 at 21:41 UTC. Arrows on the maps represent the  
 934 wind field at 150 hPa from the ECMWF analyses at 18 UTC. The white contours indicate ECMWF geopotential heights at 150  
 935 hPa.

936

937

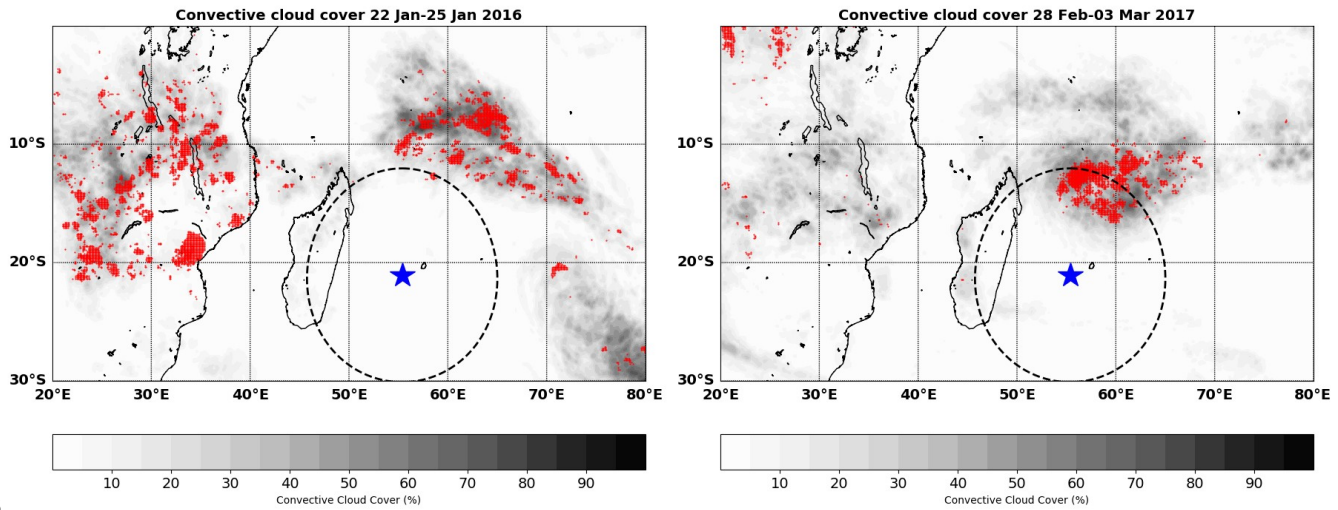
938

939

940

941

942



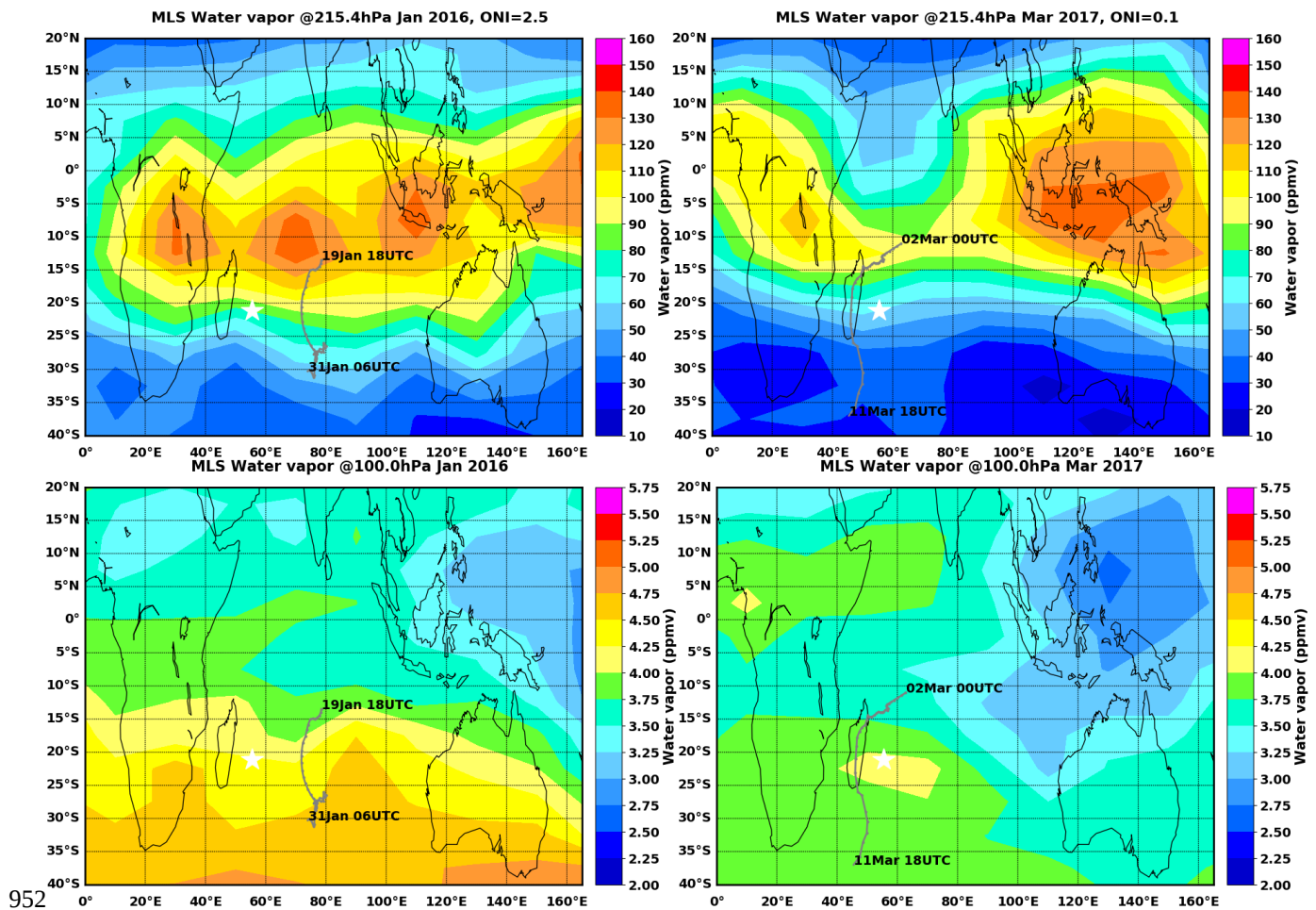
943

944 **Figure 2:** Maps of convective cloud cover (gray shading) computed using 3-hourly data of METEOSAT 7  
 945 infrared brightness temperature at 5 km resolution for 22-25 January 2016 (left) and 28 February-3  
 946 March 2017 (right). The red dots indicate pixels with the coldest tops ( $\leq 190$  K) that capture the deepest  
 947 part of convection. The dashed circle indicates a range ring of 1000 km around the Maïdo Observatory  
 948 (blue star).

949

950

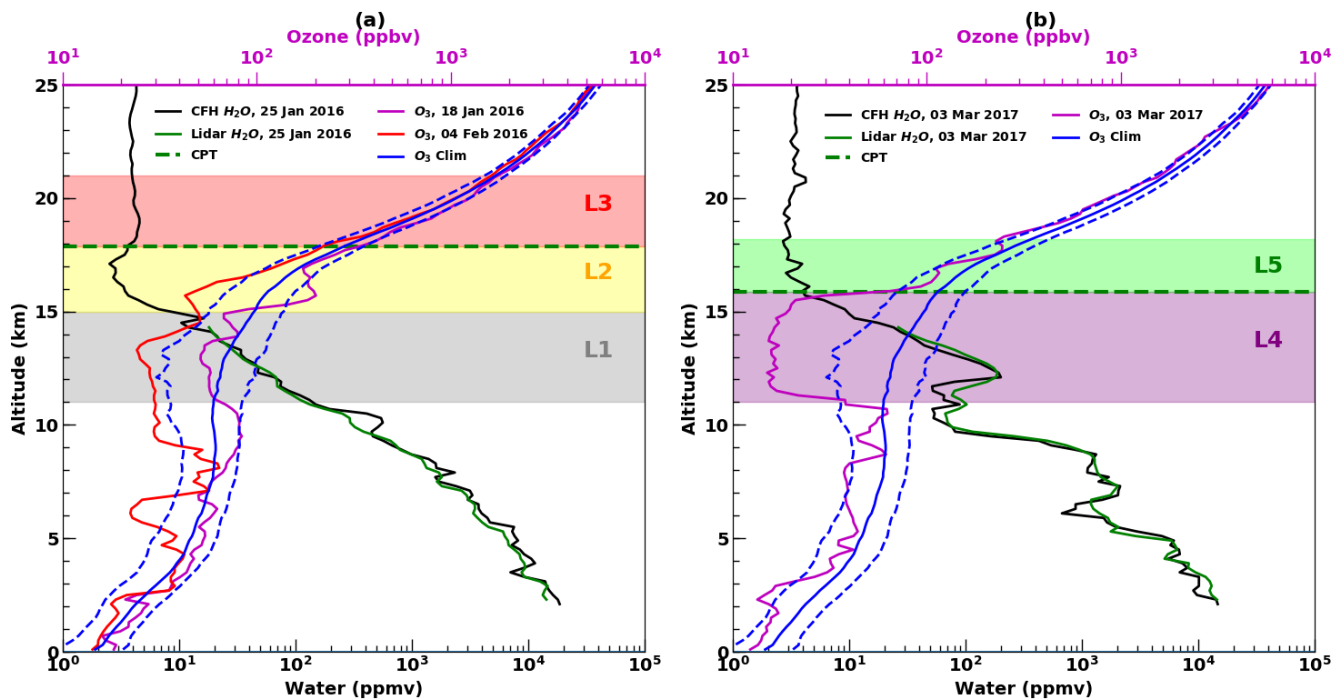
951



952

953

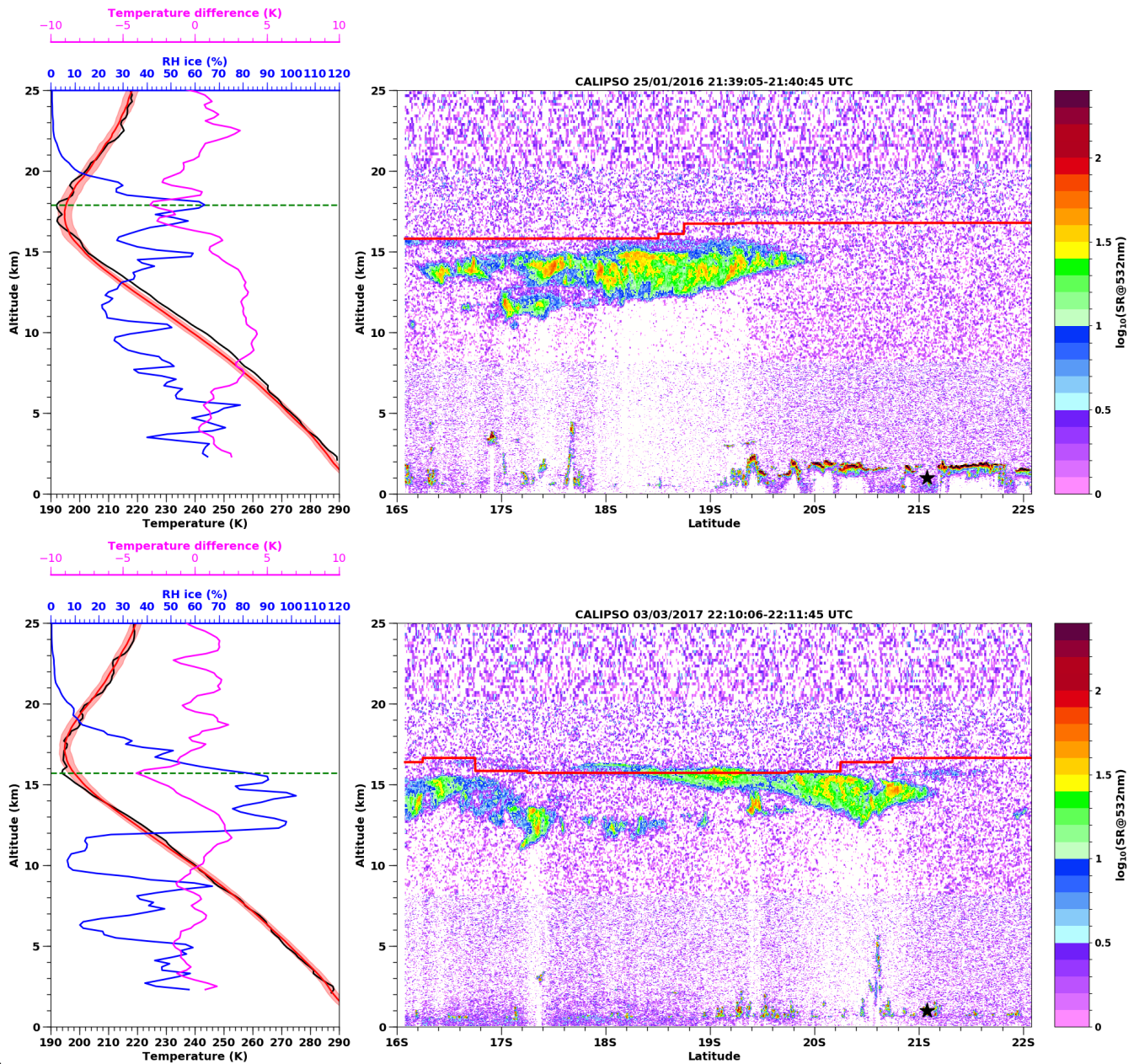
954 **Figure 3:** MLS water vapor mixing ratio (ppmv) gridded in the SWOOSH data set at 215 hPa for January 2016 (upper left)  
 955 and for March 2017 (upper right). The gray lines correspond to the best tracks of tropical cyclones Corentin (19-31 January  
 956 2016) and Enawo (02-11 March 2017). Bottom panels: same as upper panels but for 100 hPa.



957

958 **Figure 4.** Vertical profiles of: a) CFH and lidar water vapor profiles (ppmv) on 25 January 2016 (black and green line  
 959 respectively), NDACC/SHADOZ ozone profiles on 18 January 2016 (purple line) and 4 February 2016 (red line); b) CFH  
 960 and lidar water vapor profiles (black and green line respectively) and NDACC/SHADOZ ozone profile (purple line) on 3  
 961 March 2017. The location of the cold point tropopause is indicated by the dashed green line. Also shown on each plot is the  
 962 1998-2017 climatological mean ozone profile (blue line) for DJFM and the  $\pm$  one standard deviation of the climatology  
 963 corresponds to the dashed blue line. The most important layers in the water vapor/ozone profiles are shaded and named.





964

965 **Figure 5:** Top and bottom left: vertical profiles of temperature and relative humidity with respect to ice (black and blue line  
 966 respectively) measured on 25 January 2016 at 17:52 UTC and 3 March 2017 at 18:00 UTC. The green dashed line  
 967 corresponds to the cold point tropopause. The NDACC/SHADOZ climatological-mean summertime (DJFM) profile of  
 968 temperature (red line), the  $\pm$  one standard deviation (red shading) and temperature anomaly (magenta line) are also shown.

75

76

969 Top and bottom right: Latitude-altitude distribution of CALIOP backscattering ratio at 532 nm along CALIOP track near  
970 Réunion Island on 25 January 2016 (top right) and 3 March 2017 (bottom right). The mean longitude difference between the  
971 CFH profile and the CALIOP track is  $2.4^\circ$  on 25 January 2016 and  $5.3^\circ$  on 3 March 2017. The red curve on each CALIOP  
972 plot corresponds to the tropopause height provided by the GEOS 5 global model data available in the CALIPSO Level 1 data  
973 files. The latitude of the Maïdo Observatory is indicated by the black star on each CALIOP plot.

974

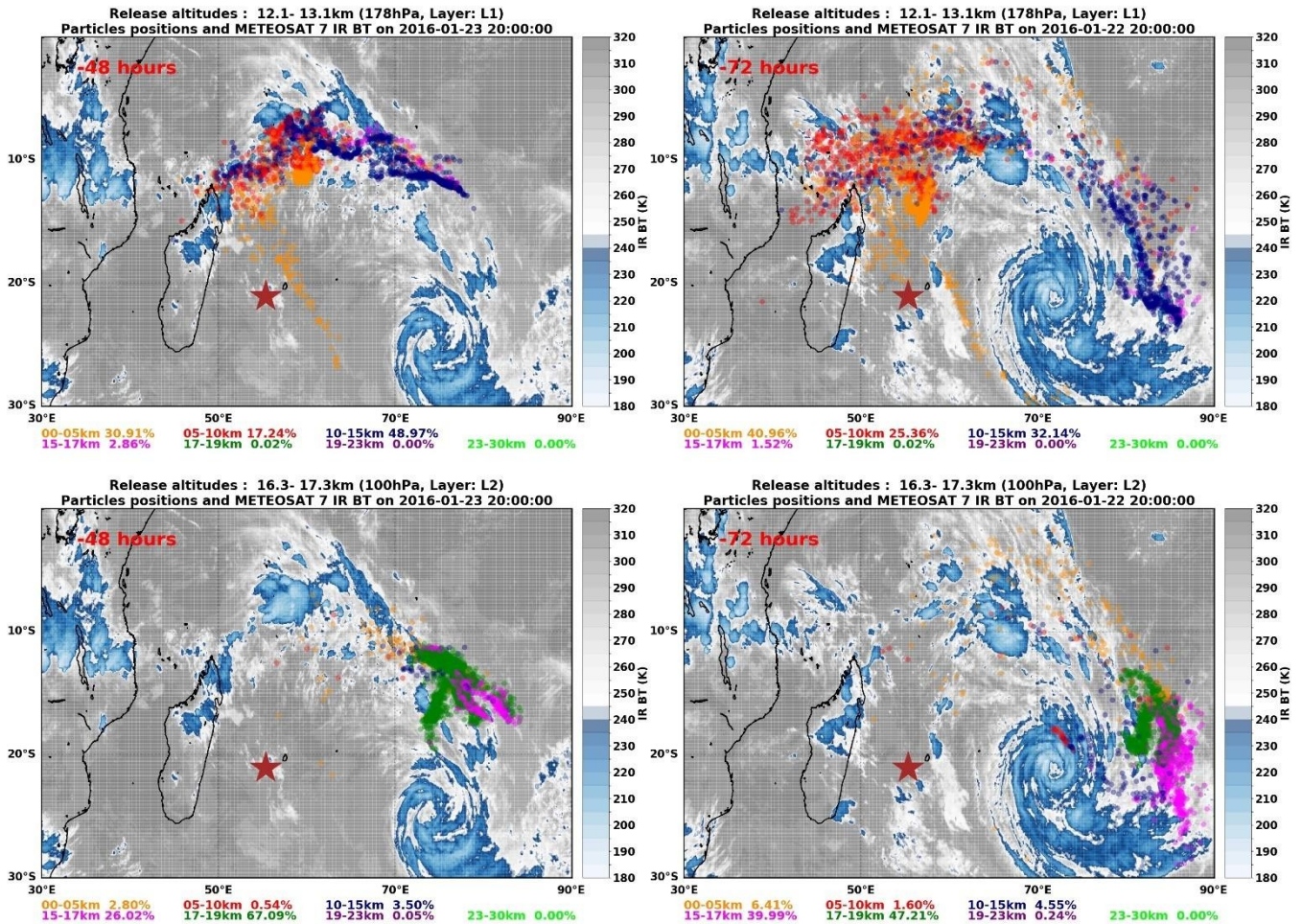
975

976

977

978

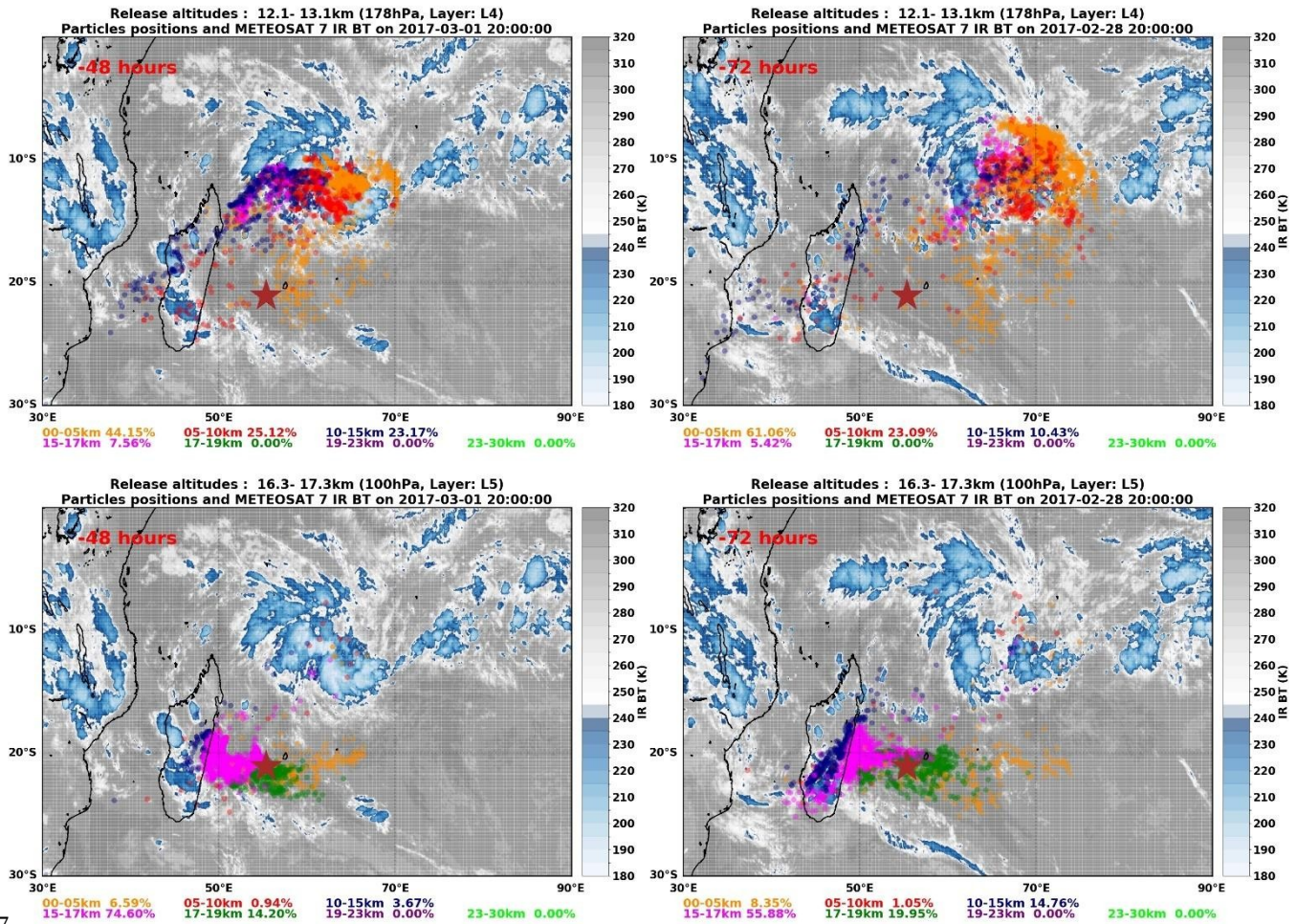
979



980

981 | **Figure 6:** Backward trajectories calculated with the FLEXPART\_ model for the CFH flight on 25 January 2016. On the  
 982 upper panel backward trajectories were initialized at 178 hPa (Layer L1) on 25 January 2016. The particle positions two days  
 983 before (on 23 January 2016 at 20 UTC, upper left) and three days before (on 22 January 2016 at 20 UTC, upper right) are  
 984 shown with respect to the METEOSAT 7 cloud distribution at those times. The altitude range of the particles (e.g. 0-5km)  
 985 and the percent of particles in that altitude range are indicated according to a color code shown on the bottom of each panel.  
 986 Bottom panel: same as upper panel but for backward trajectories initialized at 100 hPa (Layer L2) on 25 January 2016.



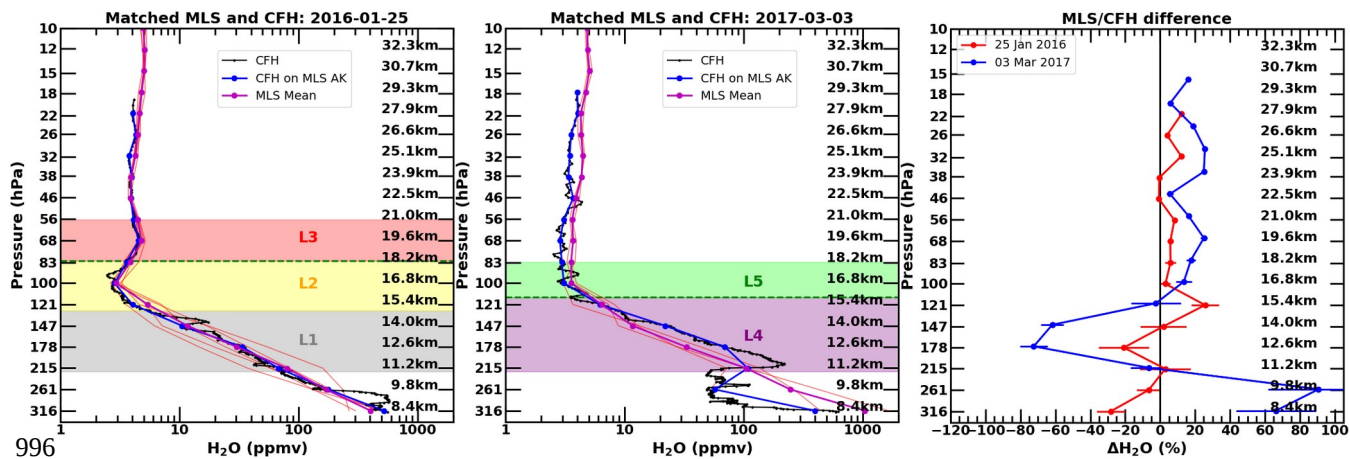


987

988 **Figure 7:** Backward trajectories calculated with the FLEXPART model for the CFH flight on 3 March 2017. On the upper  
 989 panel backward trajectories were initialized at 178 hPa (Layer L4) on 3 March 2017. The particle positions two days before  
 990 (on 1 March 2017 at 20 UTC, upper right) and three days before (on 28 February 2017 at 20 UTC, upper left) are shown  
 991 with respect to the METEOSAT 7 cloud distribution at those times. The altitude range of the particles (e.g. 0-5km) and the  
 992 percent of particles in that altitude range are indicated according to a color code shown on the bottom of each panel. Bottom  
 993 panel: same as upper panel but for backward trajectories initialized at 100 hPa (Layer L5) on 3 March 2017.

994

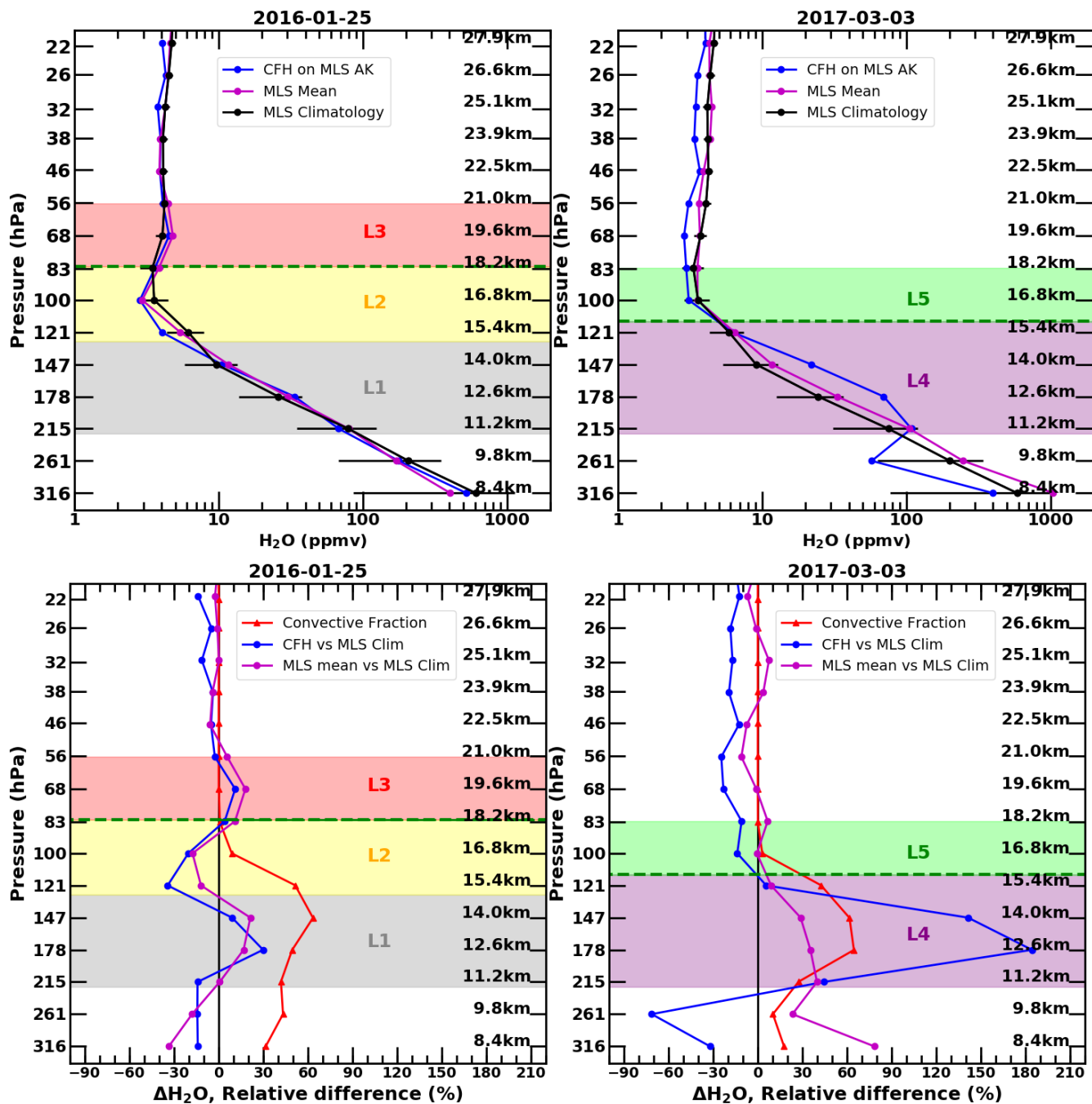
995



996

997

998 **Figure 8:** Left and middle panels: High-resolution (black line) and convolved (blue line) CFH water vapor profiles and  
 999 closest-matched MLS profiles (thin red line) on 25 January 2016 (5 profiles) and 3 March 2017 (3 profiles). The mean MLS  
 1000 profile for each date corresponds to the thick magenta line. The location of the cold point tropopause is indicated by the  
 1001 dashed green line. Important water vapor features are shaded and named. Right panel: Mean percent difference between the  
 1002 convolved CFH water vapor profile and MLS coincident profiles on 25 January 2016 (red line) and 3 March 2017 (blue  
 1003 line). The horizontal bars indicate twice the standard error of the mean percent difference. Markers for each pressure level on  
 1004 3 March 2017 are slightly offset in pressure for clarity. Corresponding altitude values for MLS pressure levels are also  
 1005 shown on each plot.



1006

1007 **Figure 9:** Upper panel: Convolved CFH water vapor profiles (blue line), mean of closest-matched MLS profiles (magenta)  
 1008 and monthly mean climatological MLS water vapor profile for Réunion Island (black line, see text for definition of the MLS

1009 climatological profile) on 25 January 2016 (upper left) and 3 March 2017 (upper right). The horizontal bars in black  
1010 correspond to the  $\pm$  one standard deviation range. Bottom panel: Relative difference between the convolved CFH water  
1011 vapor profile and the MLS climatological profile for Réunion Island (blue line) and the mean of closest-matched MLS  
1012 profiles and the MLS climatological profile (magenta line). The convective fraction computed with FLEXPART  
1013 backtrajectories and METEOSAT 7 infrared brightness temperature is shown in red. Corresponding altitude values for MLS  
1014 pressure levels are also shown on each plot.